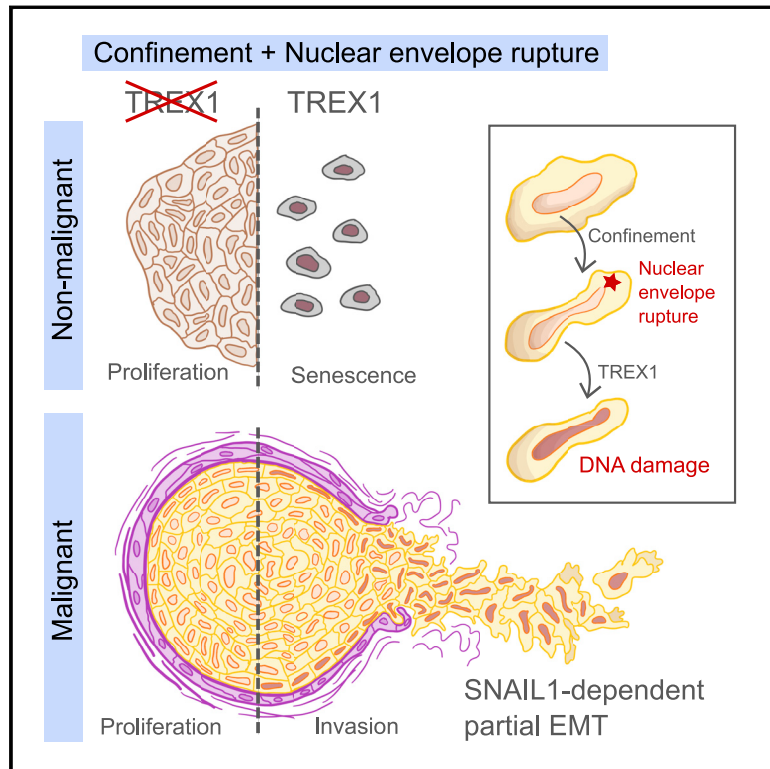Article

Compromised nuclear envelope integrity drives TREX1-dependent DNA damage and tumor cell invasion

Graphical abstract

Authors

Guilherme Pedreira de Freitas Nader, Sonia Agüera-Gonzalez, Fiona Routet, ..., Nicolas Manel, Philippe Chavrier, Matthieu Piel

Correspondence

nicolas.manel@curie.fr (N.M.),
philippe.chavrier@curie.fr (P.C.),
matthieu.piel@curie.fr (M.P.)

In brief

Extreme nuclear deformations in dense microenvironments lead to repeated nuclear envelope rupture followed by TREX1-dependent chronic DNA damage. This triggers a partial EMT in malignant cells which might underlie tumor progression.

Highlights

- Deformed nuclei and DNA damage are enriched at micro-invasive foci of breast cancer

- TREX1 causes DNA damage in deformed nuclei upon nuclear envelope rupture events

- TREX1 drives senescence in normal cells and an invasive phenotype in cancer cells

- Nuclear envelope rupture events and DNA damage are observed in human tumors

CellPress

Cell

Article

Compromised nuclear envelope integrity drives TREX1-dependent DNA damage and tumor cell invasion

Guilherme Pedreira de Freitas Nader,[1] Sonia Agüera-Gonzalez,[2] Fiona Routet,[2] Matthieu Gratia,[3] Mathieu Maurin,[3] Valeria Cancila,[4] Clotilde Cadart,[1,11] Andrea Palamidessi,[8,9] Rodrigo Nalio Ramos,[10] Mabel San Roman,[3] Matteo Gentili,[3,12] Ayako Yamada,[5,13] Alice Williart,[1] Catalina Lodillinsky,[6,7] Emilie Lagoutte,[2] Catherine Villard,[5] Jean-Louis Viovy,[5] Claudio Tripodo,[4] Jérôme Galon,[10] Giorgio Scita,[8,9,14] Nicolas Manel,[3,14,*] Philippe Chavrier,[2,14,*] and Matthieu Piel[1,14,15,*]

[1]Institut Curie and Institut Pierre Gilles de Gennes, PSL Research University, CNRS, UMR 144, Paris, France
[2]Institut Curie, PSL Research University, CNRS, UMR 144, Paris, France
[3]Institut Curie, PSL Research University, INSERM, U932, Paris, France
[4]Tumor Immunology Unit, University of Palermo, Corso Tukory 211, 90234 Palermo, Italy
[5]Institut Curie, Université PSL, CNRS, UMR 168, Paris, France
[6]Research Area, Instituto de Oncología Ángel H. Roffo, Universidad de Buenos Aires, Buenos Aires, Argentina
[7]Consejo Nacional de Investigaciones Científicas y Técnicas (CONICET), Buenos Aires, Argentina
[8]FIRC Institute of Molecular Oncology, IFOM, Via Adamello 16, 20139 Milano, Italy
[9]Department of Oncology and Hemato-Oncology, University of Milan, IFOM, Via Adamello 16, 20139 Milano, Italy
[10]INSERM, Sorbonne Université, Université de Paris, Equipe Labellisée Ligue Contre le Cancer, Centre de Recherche des Cordeliers, Laboratory of Integrative Cancer Immunology, Paris, France
[11]Present address: Department of Molecular and Cell Biology, University of California, Berkeley, CA 94720-3200, USA
[12]Present address: Broad Institute of MIT and Harvard, 415 Main Street, Cambridge, MA 02142, USA
[13]Present address: PASTEUR, Département de chimie, École normale supérieure, Université PSL, Sorbonne Université, CNRS, Paris, France
[14]These authors contributed equally
[15]Lead contact
*Correspondence: nicolas.manel@curie.fr (N.M.), philippe.chavrier@curie.fr (P.C.), matthieu.piel@curie.fr (M.P.)
https://doi.org/10.1016/j.cell.2021.08.035

SUMMARY

Although mutations leading to a compromised nuclear envelope cause diseases such as muscular dystrophies or accelerated aging, the consequences of mechanically induced nuclear envelope ruptures are less known. Here, we show that nuclear envelope ruptures induce DNA damage that promotes senescence in non-transformed cells and induces an invasive phenotype in human breast cancer cells. We find that the endoplasmic reticulum (ER)-associated exonuclease TREX1 translocates into the nucleus after nuclear envelope rupture and is required to induce DNA damage. Inside the mammary duct, cellular crowding leads to nuclear envelope ruptures that generate TREX1-dependent DNA damage, thereby driving the progression of *in situ* carcinoma to the invasive stage. DNA damage and nuclear envelope rupture markers were also enriched at the invasive edge of human tumors. We propose that DNA damage in mechanically challenged nuclei could affect the pathophysiology of crowded tissues by modulating proliferation and extracellular matrix degradation of normal and transformed cells.

INTRODUCTION

In tissues, extracellular matrix fibers and cell packing limit the available space. Migrating and proliferating cells thus often face situations of crowding and confinement, which can result in strong cell and nucleus deformations. We and others showed that, in the case of migrating immune and cancer cells, strong nuclear deformation can result in transient events of nuclear envelope (NE) rupture with subsequent DNA damage (Denais et al., 2016; Hatch, 2018; Hatch and Hetzer, 2016; Irianto et al., 2017; Raab et al., 2016). In this context, efficient repair responses are essential to ensure cell viability, which involve ESCRT proteins restoring NE integrity, as well as BAF1 and the DNA repair pathways (Lusk and Ader, 2020). NE ruptures can be induced by sim-

ply confining cells between two plates, independently of their migratory behavior (Le Berre et al., 2012; Gentili et al., 2019; Hatch and Hetzer, 2016). They can also occur spontaneously in fragile mutant nuclei (Vargas et al., 2012; De Vos et al., 2011), associated with a large range of degenerative diseases (Robijns et al., 2018). Recent studies showed that NE rupture events also occur *in vivo*, for example in muscle tissues that are highly solicited mechanically but also in the heart of developing embryos, due to stiffening and beating of the tissue (Cho et al., 2019), as well as in skeletal muscle cells harboring mutations in the lamin A/C gene, due to forces exerted on the nuclei by the microtubule cytoskeleton (Earle et al., 2020; Roman et al., 2017). In these tissues, NE ruptures are associated with senescence and aging phenomena that affect cell proliferation,
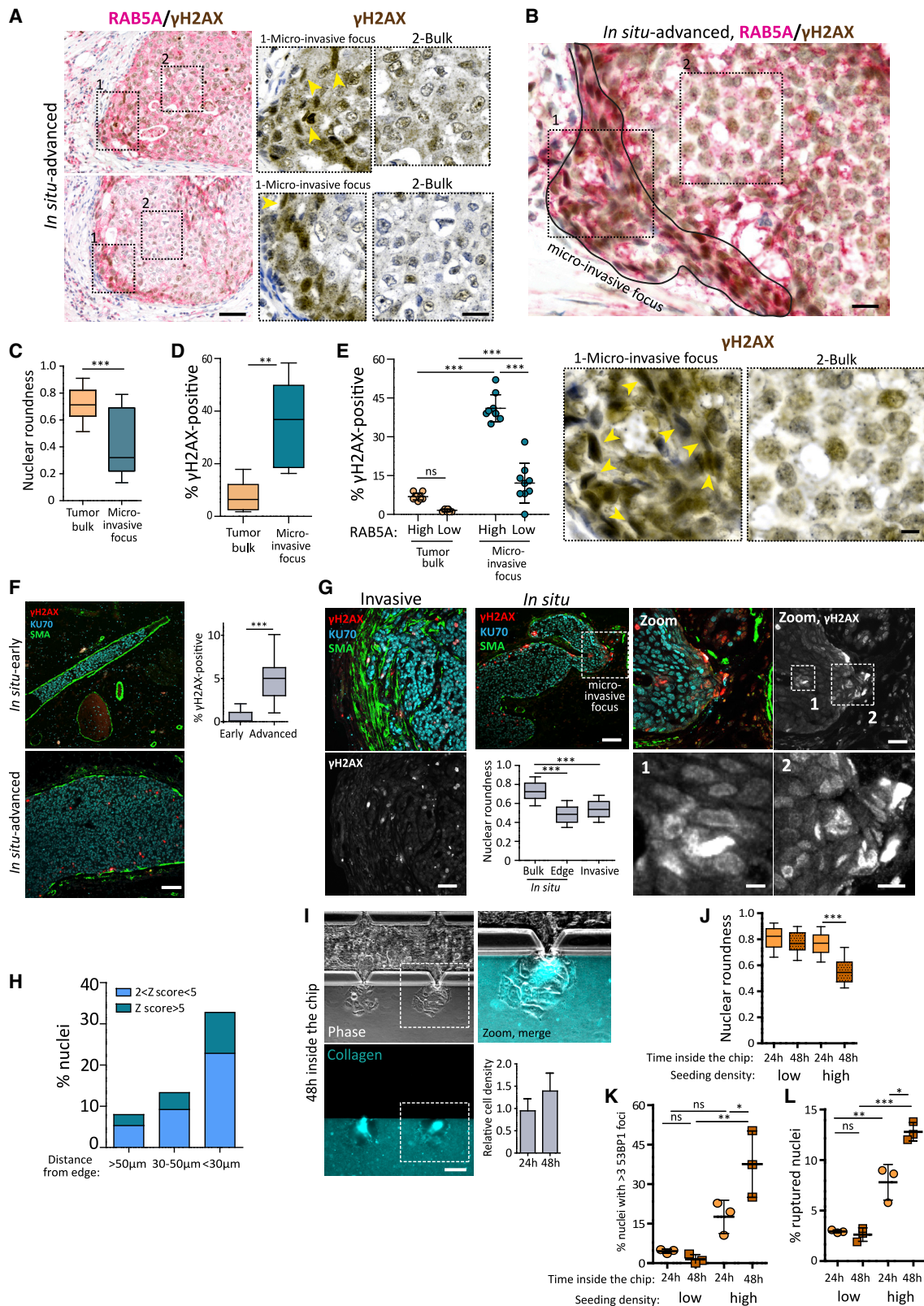
(legend on next page)

survival, and ultimately tissue function. NE ruptures are often accompanied by DNA damage (Cho et al., 2019; Denais et al., 2016; Earle et al., 2020; Feng et al., 2018; Raab et al., 2016). Mechanisms leading to senescence and DNA damage upon NE rupture are unclear. Here, we investigated the consequences of nuclear deformation and rupture associated with cell migration in crowded tissues, focusing on mammary carcinoma. These tumors, which grow confined inside the mammary ducts, have been shown to display large strands of collectively moving cells associated with the transition from *in situ* to the invasive stage of the tumor development (Palamidessi et al., 2019). Additionally, the breast neoplastic invasive switch requires the activity of matrix proteases for breaching out of the duct (Feinberg et al., 2018; Lodillinsky et al., 2016).

RESULTS

We first investigated human samples of breast ductal adenocarcinoma *in situ* with microinvasion stained by immunohistochemistry for the small GTPase RAB5A (involved in recycling of cell/cell adhesions) used as a marker for strands of motile cells (Malinverno et al., 2017) and the DNA damage marker phospho-γH2AX. We observed that tumor regions positive for RAB5A, often corresponding to micro-invasive foci (STAR Methods; Kim et al., 2018), displayed a larger number of deformed and elongated nuclei (Figures 1A–1E). This morphology corresponds to cells squeezing each other as they move (Friedl and Gilmour, 2009; Palamidessi et al., 2019). Nuclei positive for γH2AX were more abundant in invasive foci than in the tumor bulk (Figure 1D), and within invasive foci, γH2AX-positive nuclei were more often found in cells with higher RAB5A expression (presumably more migratory) (Palamidessi et al., 2019; Figure 1E). This suggests that strands of motile cells at the periphery of the tumor exhibit pronounced nuclear deformation associated with elevated DNA damage.

We then investigated a xenograft mouse model based on the intraductal (intra-nipple) injection of transformed human breast cancer MCF10DCIS.com (DCIS hereafter) cells, which are derived from the non-tumorigenic breast epithelial MCF10A cell line. This model recapitulates the transition from *in situ* to invasive stages of breast cancer progression (Behbod et al., 2009; Lodillinsky et al., 2016). *In situ* tumors are characterized by a myoepithelial layer (stained with smooth muscle actin) surrounding human xenografted cells (identified by a human-specific KU70 antibody) (Figure 1F). Tumor sections were stained with γH2AX (Figures 1F and 1G). Advanced tumors (classified based on the state of the myoepithelial layer) displayed more γH2AX-positive nuclei (Figure 1F). Deformed nuclei were mostly found at the periphery of the tumor mass, especially in ducts inflated with large tumors, and enriched in micro-invasive foci (Figure 1G). Most of the γH2AX-positive nuclei did not correspond to mitotic nor apoptotic figures (Figure S1A), which were excluded from the analysis. We performed an automated analysis of all human nuclei in the tumor regarding their level of γH2AX staining, as a function of their distance to the tumor edge (Figure S1A for the method). This analysis showed enrichment for nuclei with an elevated γH2AX staining (Z score above 2) and even more for nuclei with a very high staining (Z score above 5) in the region closer to the tumor edge (Figures 1H and S1B). Together, these data show that the periphery of mammary *in situ* carcinomatous lesions, both in human and in xenografted mice, often display strongly deformed nuclei with elevated levels of DNA damage. This raises the possibility that NE ruptures could be implicated in the induction of the DNA damage, as suggested by previous work on migrating cells (Denais et al., 2016; Raab et al., 2016).

Because NE ruptures of deformed nuclei were difficult to investigate in tumor samples, we developed a "duct-on-chip" microfluidic assay (inspired by Blaha et al. [2017]). The assay consists of three large 50-μm high channels: a lateral channel

Figure 1. Human breast tumor and mouse xenograft model of breast cancer progression display strong nuclear deformation and DNA damage

(A) Immunohistochemistry of *in situ* advanced human primary breast tumors. RAB5A (red), γH2AX (brown). Bar, 80 μm.

(B) Magnified region of *in situ* advanced primary breast tumor with a micro-invasive focus. Yellow arrowheads point to deformed nuclei. Bar, 25 μm.

(C and D) Box and whisker plot showing the median value and 10–90 percentiles of (C) nuclear roundness index or (D) γH2AX-positive nuclei.

(E) Bars are the mean ± SD of 6 individual tumor samples where at least 150 nuclei were scored per sample.

(F and G) Immunofluorescence analysis of alpha-smooth muscle actin (green), human-specific KU70 (cyan), and γH2AX (red) in 7-week-old mouse xenografts at different stages generated by intraductal injection of DCIS cells. (F) The *in situ*-advanced stage is characterized by a discontinuous/broken myoepithelial layer. Graph, box and whisker plot showing the median value and 10–90 percentiles of γH2AX-positive nuclei measured at *in situ*-early and *in situ*-advanced stages. Data represent 3 independent experiments where 500 nuclei were scored per tumor stage, per experiment. (G) Invasive stage: SMA-positive and elongated cells represent cancer-associated fibroblasts. Graph, box and whisker plot showing the median value and 10–90 percentiles of the nuclear roundness index measured at invasive and *in situ* stages (divided into edge-up to 2 cell layers below the myoepithelial layer and bulk). Data represent 3 independent experiments where 7 *in situ* and 13 invasive tumor samples were analyzed (for a total of 140 nuclei analyzed for *in situ*-bulk, 139 nuclei analyzed for *in situ*-edge, and 264 nuclei analyzed for invasive tumor samples).

(H) Classification of Z scores categories (γH2AX intensities) of nuclei as a function of different distances from the tumor edge (determined by the myoepithelial layer) (for details refer to Figure S1A). Data represent a total of 23 images analyzed for DCIS parental tumors from 3 independent mice injections.

(I) Duct-on-chip assay. Cell density was measured by counting the number of cells/μm^2 in 5 random fields (20× magnification) at the indicated time points and are expressed in the graph relative to the 24-h time point. Data represent the mean ± SD of 3 independent experiments. Bar, 50 μm; zoom bar, 25 μm.

(J–L) Duct-on-chip assay. DCIS cells stably expressing 53BP1-mCherry and cGAS-EGFP were injected into the duct-on-a chip device at low and high density. Nuclear roundness (J), DNA damage (K), and NE rupture (L) were assessed. Graphs: (J) box and whisker plot showing the median value and 10–90 percentiles of the nuclear roundness. (K and L) Bars are the mean ± SD of 3 independent experiments. p values were calculated by unpaired Student's t test, except for items (E) and (K) (one-way ANOVA with post hoc Tukey test) and item (L) (χ^2 test). ***p < 0.0001; **p < 0.005; *p < 0.05; ns, not significant.

(A–D) Representative of 7 independent tumor samples where 21 and 27 nuclei were analyzed for tumor bulk and micro-invasive focus, respectively, per sample. (F and G) Bar, 100 μm; (G) zoom bar, 50 μm; inset bars, 15 μm.

See also Figure S1 and Video S1.
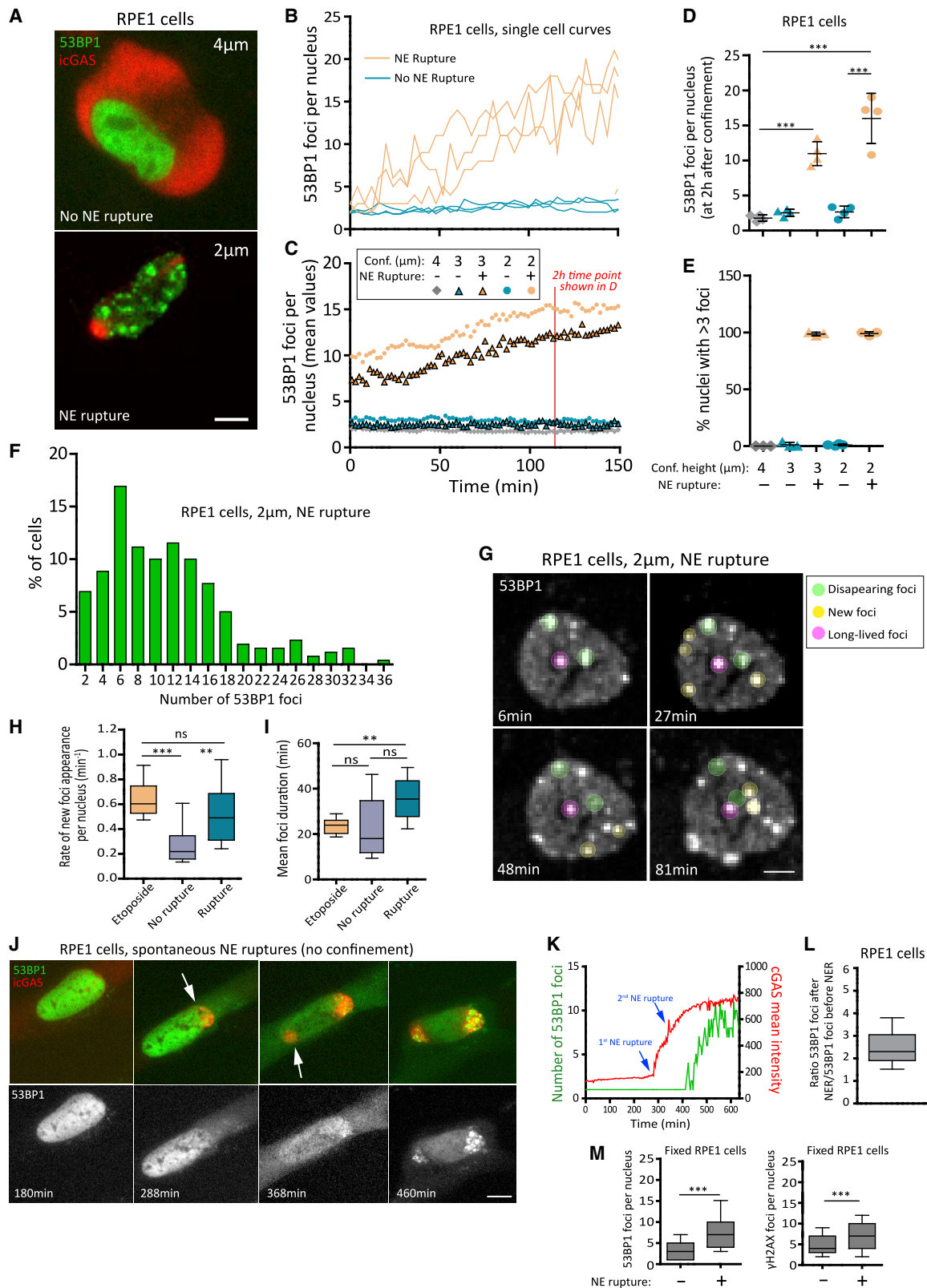
filled with culture medium, a central one with DCIS cells, and the third channel with a dense fluorescently labeled type I collagen fibrillar matrix. The channels are connected by regularly spaced V-shape gates, 10 μm-wide in their smaller section, through which cells can migrate toward the collagen-filled chamber (Figures 1I and S1C). Cells invaded efficiently the collagen chamber (Figure 1I), and visualization of the collagen network suggested that they were able to remodel the collagen fibers over time (Figure 1I). Using a pan inhibitor of matrix metalloproteinases (MMPs), GM6001, we confirmed that collagen degradation by DCIS cells was required for invasion into the collagen chamber (Figures S1D and S1E), similar to what we had previously observed in vivo (Lodillinsky et al., 2016). DCIS cells expressing catalytically inactive cGAS-mCherry (icGAS hereafter) to detect NE ruptures (Gentili et al., 2019; Raab et al., 2016) and 53BP1-GFP to detect DNA double-strand break (DSB) foci were grown in the device. The average cell density increased by 50% from 24 h to 48 h after cell loading (Figure 1I). The device was loaded either with a low or a high density of cells (Figures S1F–S1H), so that, after 48 h, the low-seeding density would remain below the initial high-seeding density. We then quantified the shape of nuclei, the number of 53BP1-GFP foci, and the fraction of nuclei showing icGAS-mCherry peripheral accumulation, characteristic of NE rupture events (Figure S1H; Raab et al., 2016). 48 h after seeding at high density, but not at low density, nuclear roundness decreased, indicating that nuclei were getting confined and deformed (Figure 1J), and the fraction of nuclei with NE ruptures and elevated 53BP1 foci (>3) increased (Figures 1K and 1L). DCIS cells remained motile even at high density (Video S1; Malinverno et al., 2017; Palamidessi et al., 2019). This suggests that, similarly to what was observed for single migrating cells in a dense tissue (Denais et al., 2016; Raab et al., 2016), the motility of DCIS cells in a crowded multicellular context can lead to nuclear deformation, NE rupture, and DNA damage.

To examine the link between nuclear deformation, NE rupture, and DNA damage, we used a 2D confiner device that allows precise deformation of cells (and nuclei) between two parallel plates (Le Berre et al., 2014). In addition to DCIS cells, we analyzed the non-tumorigenic cell lines RPE1 (normal human hTERT immortalized cells) in which we have previously characterized NE ruptures and DNA d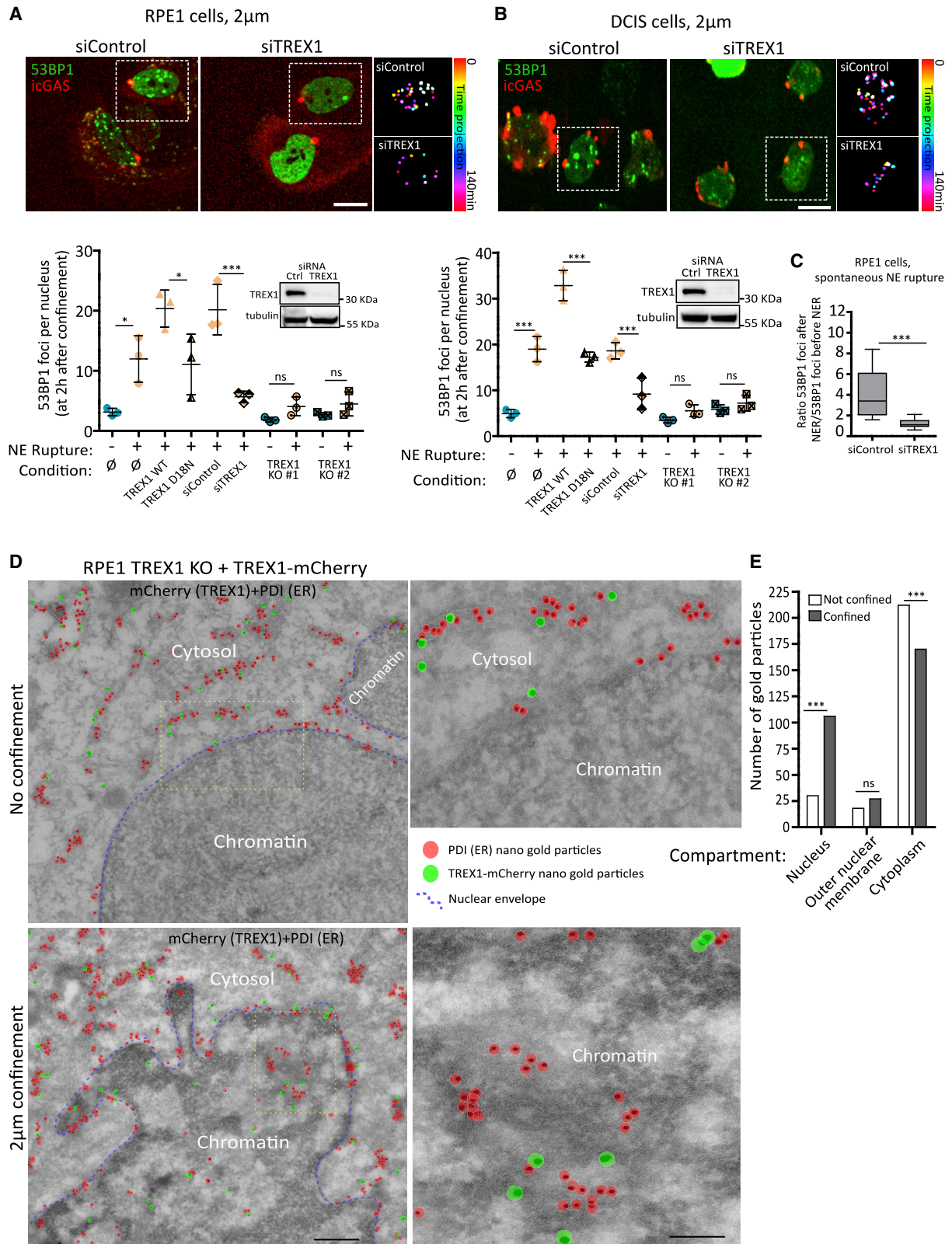amage in migration assays (Raab et al., 2016) and MCF10A expressing icGAS-mCherry and 53BP1-GFP (Figure 2A). We found a sharp increase in the fraction of RPE1 cells with ruptured nuclei below 3 μm confinement (Figures S2A and S2B), confirming our previous observations on another panel of cell types (Raab et al., 2016). To assess the relationship between NE rupture and DNA damage, we analyzed the number of 53BP1-GFP foci in nuclei of cells confined at various heights and displaying or not displaying NE ruptures (Figure S2A). Foci were counted at each time point using a semi-automated process (Figure S2C; STAR Methods). We found that, similarly to cells migrating through constrictions (Raab et al., 2016), only cells with ruptured NE displayed increased number of 53BP1 foci (Figures 2B–2D for RPE1 and Figure S2D for DCIS and MCF10A). Almost all cells with NE rupture (>98%) displayed more than three 53BP1 foci (Figures 2E and 2F), whereas only a small fraction of cells without NE rupture (<2%) had this number of foci over the course of the video (Figure 2E). Analysis of the intensity of foci and of the background (Figure S2E) showed that 53BP1 accumulated in an increasing number of foci in nuclei with NE ruptures. Cells exhibiting NE ruptures were also positive for other markers of DNA damage, such as RIF1 and γH2AX (Figures S2F and S2G). Additionally, the number of 53BP1 foci per nucleus did not depend on the cell cycle (Figure S2H). Collectively, these results indicate that confinement-induced DNA damage was preceded by NE rupture events in a variety of cells, including RPE1 (in accordance with other reports) (Raab et al., 2016; Shah et al., 2021), MCF10A, and DCIS cells.

In cells displaying NE ruptures, the number of 53BP1 foci remained high throughout the confinement period (Figures 2C and S2D) and was associated with a majority of cells showing repeated cycles of NE blebbing, rupture, and repair over the entire duration of confinement, in contrast to cells confined at 4 μm (Video S2). These resuls suggest that the occurrence of DNA damage associated with deformed nuclei in the human tumor samples could correspond to repeat NE ruptures.

Previous work suggested that NE rupture might lead to DNA repair proteins leaking out of the nucleus (Irianto et al., 2017). Some cytoplasmic factor(s) might also enter the nucleus and access nuclear DNA, causing DNA damage (Maciejowski et al., 2015, 2019; Shah et al., 2017). Live recording of 53BP1-GFP showed the expected dynamic appearance and disappearance

Figure 2. Strong confinement induces NE rupture leading to DNA damage

(A) Cells stably expressing 53BP1-EGFP and catalytically inactive cGAS-mCherry (icGAS) were confined and images were taken after 2 h. Bar, 5 μm.

(B) Single cell curves of 53BP1 foci number as a function of time in cells displaying or not NE rupture while under 2 μm confinement.

(C) Quantification of DNA damage level during confinement. Data represent the mean ± SD of 4 independent experiments where 20 cells per experiment per condition were analyzed.

(E) Quantification of the percentage of cells displaying more than 3 53BP1 foci/nucleus while confined at 2 μm.

(F) Frequency distribution of 53BP1 foci number/nucleus in cells displaying NE rupture. Data represent 250 nuclei pooled from 3 independent experiments.

(G) Illustrative panels depicting the appearance and repair of DNA damage foci in cells stably expressing 53BP1-EGFP while confined at 2 μm. Bar, 5 μm.

(H and I) Frequency of foci appearance and foci life-time (foci duration) in RPE1 cells confined at 2 μm or treated with etoposide (25 μM). Box and whisker plot show the median value and 10–90 percentiles of 3 independent experiments where 20 cells per condition per experiment were analyzed.

(J) Cells stably expressing 53BP1-EGFP and icGAS were plated on glass bottom dishes and imaged for several hours. Arrows point to NE rupture events.

(K) Single cell curves showing the relationship between NE rupture and the appearance of 53BP1 foci.

(L) Box and whisker plot showing the median value and 10–90 percentiles of the ratio between the number of 53BP1 foci after and before NE rupture. Data are from 2 independent experiments where 10 NE rupture events per experiment were analyzed.

(M) Cells stably expressing 53BP1-EGFP and icGAS were confined at 2 μm, harvested and plated for 20 min before fixation for immunostaining with antibodies against GFP (left) or γH2AX (right); box and whisker plot show the median value and 10–90 percentiles. p values were calculated by unpaired Student's t test except for (H) and (I) (one-way ANOVA with post hoc Tukey test). ***p < 0.0001; **p < 0.005; ns, not significant.

See also Figure S2 and Videos S2 and S3.

A RPE1 cells, 2μm

B DCIS cells, 2μm

C RPE1 cells, spontaneous NE rupture

D RPE1 TREX1 KO + TREX1-mCherry

E

(legend on next page)

of single foci, indicative of DNA damage and repair events (Figure 2G; Video S2). We found that the frequency of appearance of new foci was significantly higher in cells with NE rupture in comparison with cells without NE rupture, reaching rates comparable to etoposide-treated cells (Figure 2H). Moreover, the number of new foci typically increased after a rupture event (Figures S2I and S2J), suggesting a causal relationship between NE rupture and new DNA damage. On the contrary, lifetime of the foci showed no difference between cells with or without NE ruptures (Figure 2I). Overall, these experiments suggest that DNA damage associated with NE ruptures is mostly due to the generation of new DNA damage following NE rupture events rather than to delayed repair.

To investigate whether DNA damage was solely associated to NE rupture events or whether cell and nuclear confinement were also required, we recorded non-confined cells plated on a glass coverslip. In these conditions, although very rare, spontaneous NE rupture events could be observed. Such events displayed a similar signature in terms of icGAS accumulation at a local site on the nuclear periphery and leakage of 53BP1-GFP staining in the cytoplasm before re-import into the nucleus (Figure 2J; Video S3). Each NE rupture event was followed, within 1–2 h, by an increase in the number of 53BP1-GFP foci in the nucleus (Figures 2J–2L). To investigate a larger population of cells, we fixed the cells and counted the number of foci using 53BP1-GFP (Figure 2M, left) or γH2AX staining (Figure 2M, right) in cells with or without NE rupture (assessed by the presence of an icGAS perinuclear accumulation). The increase in the number of foci appeared similar to the one observed after confinement-induced NE ruptures. Together, these experiments indicate that DNA damage follows NE rupture events even in the absence of confinement.

NE ruptures at persistent post-mitotic chromatin bridges have been shown to cause DNA damage, which was reduced upon depletion of TREX1, a cytoplasmic endoplasmic reticulum (ER) membrane-associated exonuclease (Maciejowski et al., 2015). We silenced TREX1 by small interfering RNA (siRNA)-mediated knockdown, or permanently knocked it out by CRISPR-Cas9 technology (in RPE1 and DCIS cells) (Figures S3A and S3B). We found that upon TREX1 depletion in the three cell lines (RPE1, MCF10A, and DCIS), NE ruptures were no longer accompanied by an increase in 53BP1 foci (Figures 3A, 3B, S3C and S3D, quantified by an independent method in S3E). TREX1 depletion also prevented the occurrence of DNA damage upon spontaneous NE rupture events in RPE1 cells (Figures 3C,

S4A, and S4B). 53BP1 foci mean intensity (Figure S3F), the generation of foci upon etoposide treatment (Figure S3G), and NE rupture frequency (Figure S3H) were not affected. WT TREX1, but not a catalytically deficient mutant (TREX1-D18N) (Lehtinen et al., 2008), increased the number of foci in cells with NE ruptures (Figures 3A and 3B). These experiments unambiguously demonstrate a role for TREX1 in promoting DNA damage upon NE rupture events in this panel of cell lines.

To determine how TREX1 gains access to nuclear DNA upon NE rupture events, we imaged TREX1-GFP expressing cells. In non-confined cells, TREX1-GFP was mostly bound to endomembranes and excluded from the nucleoplasm. Upon confinement, TREX1-GFP foci were also found inside the nucleus (Figure S3I; Video S4). Immunoelectron microscopy using gold immunolabeling against mCherry on RPE1 TREX1 knockout (KO) cells reconstituted with TREX1-mCherry showed that, in non-confined cells, gold particles were found at ER membranes distributed throughout the cytosol, co-localizing with the ER-resident enzyme, protein disulfide isomerase (PDI) (Figures 3D and S4C). PDI and TREX1 staining were increased inside the nucleus in 2-μm confined cells (Figures 3D 3E, and S4C). TREX1 was particularly enriched at the inner nuclear membrane of confined cells (Figure S4C; Tables S1 and S2; Mayhew, 2011). When localized inside the nucleus, TREX1-mCherry appeared associated to ER-like membranes together with PDI (Figure 3D). The presence of such intranuclear ER-like membranes was almost never observed in non-confined cells. These experiments suggest that, upon strong confinement at heights at which cells undergo NE rupture events, TREX1 relocalizes, along with other ER-bound proteins like PDI, from cytosolic ER to the inner side of the nuclear membrane and the inside of the nucleus, mostly bound to membranes.

Because TREX1 is an ER membrane protein and based on the immunoelectron microscopy results, we hypothesized that TREX1 might access the chromatin by diffusion from the ER membrane to connected intra-nuclear membranes (Ungricht and Kutay, 2015). Accordingly, although WT TREX1 fully rescued the level of DNA damage induced by NE rupture in TREX1 KO DCIS cells, the DeltaC construct, lacking the C-terminal ER-binding site of the protein, failed to do so (Figures S3J and S3K). A construct in which the C terminus of the protein was replaced by the ER binding site of Sec61 (Mohr et al., 2021) was able to partially rescue the level of DNA damage induced by confinement in TREX1 KO DCIS cells (Figures S3J and S3K), similarly to what was observed in micro-nuclei (Mohr et al.,

Figure 3. DNA damage upon NE rupture is TREX1-dependent

(A and B) A variety of TREX1-deficient or -proficient cells was confined at 2 μm and DNA damage level was assessed after 2 h under confinement. Graphs represent the mean ± SD of 3 independent experiments where 20 cells were analyzed per condition per experiment. Western blots: TREX1 depletion 48 h post-knockdown; tubulin is the loading control. Bar, 10 μm.

(C) Box and whisker plot showing the median value and 10–90 percentiles of the ratio between the number of 53BP1 foci after and before NE rupture in siRNA-treated cells. Data are from 2 independent experiments where 15 cells per experiment were analyzed.

(D) Immuno-gold electron microscopy images of RPE1 TREX1 KO cells reconstituted with TREX1-mCherry, confined at 2 μm or left unconfined. Bar, 0.5 μm; magnified regions bar, 0.1 μm.

(E) Number of mCherry (TREX1) immune gold particles at the indicated cellular compartments (see also Figure S5C). The "cytoplasm" compartment also includes particles associated to cytoplasmic endomembranes like ER and MVBs. p values were calculated by one-way ANOVA with post hoc Tukey test, except for (C), which was calculated by unpaired Student's t test. *p < 0.05; ***p < 0.0001; ns, not significant. Statistical significance was calculated by χ^2 test; *** does not refer to p value but significance according to the χ^2 statistics (see Table S1).

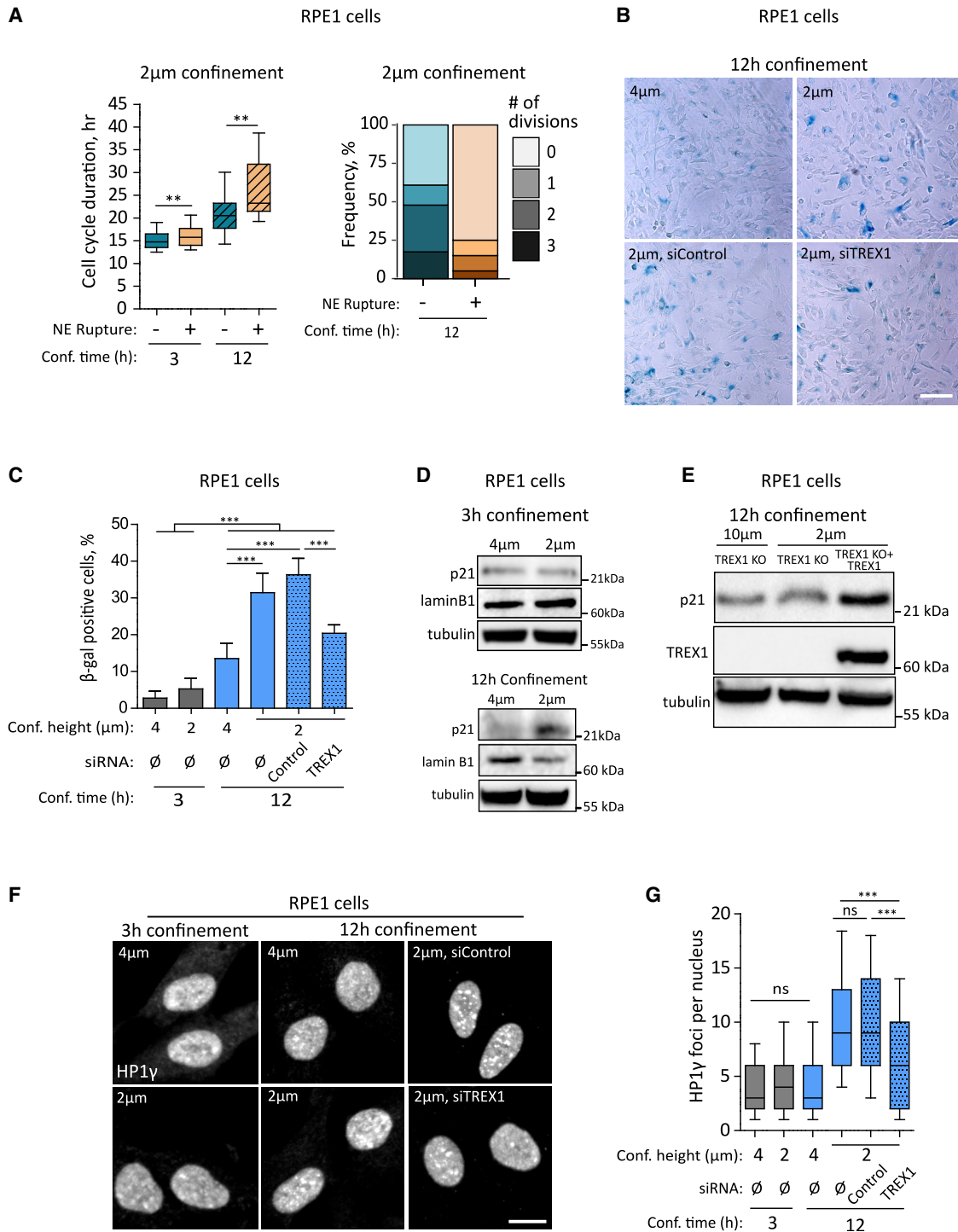See also Figures S3 and S4, Tables S1 and S2, and Video S4.

Figure 4. Long-term, strong confinement causes TREX1-dependent cell senescence

(A) Cells stably expressing catalytically inactive cGAS were confined at 2 μm for 3 or 12 h. Cells were then harvested and replated for imaging for cell cycle duration assessment in cells displaying or not NE rupture. Graphs, left: box and whisker plot showing the median value and 10–90 percentiles of the cell-cycle duration. Data for 3 h of confinement represent 3 independent experiments where a total of 150 cells with non-ruptured and 200 cells with ruptured nuclei were analyzed. Data for 12 h of confinement represent 3 independent experiments where a total of 23 lineages with non-ruptured and 40 lineages with ruptured nuclei were analyzed. Right: frequency distribution of the number of cell divisions.

(B, C, F, and G) siRNA-treated cells were confined, then harvested, replated, and cultured for 72 h before fixation for β-gal staining (B and C) or immunostaining of heterochromatin foci (HP1γ) (F and G). (C) Data represent the mean ± SD of 3 independent experiments where 200 cells were scored per condition per experiment.

(legend continued on next page)

2021). Together, these experiments suggest that upon NE rupture events, ER-bound TREX1 gains access to the interior of the nucleus causing DNA damage.

Having established a mechanism of DNA damage generation after NE rupture, we next sought to examine the functional consequences of this damage. In non-transformed cells, chronic exposure to DNA damage-inducing factors is associated with cellular senescence. RPE1 and MCF10A cells showed a very clear induction of senescence upon treatment with etoposide and doxorubicin (hereafter referred to as doxo) as verified by senescence-associated-β-galactosidase (β-gal)-positive staining. However, senescence was less pronounced in the tumorigenic DCIS cells (Figure S5A). During confinement, even for long confinement periods, most of the cells did not undergo mitosis nor showed any sign of death (Figures S5B and S5C). Following confinement, cells were harvested and replated in order to track single cells that had ruptured their NE or not based on icGAS perinuclear staining/distribution (Figure S5D). After a short period of confinement (2 h), de-confined cells resumed proliferation with an almost normal cell-cycle duration (Figure 4A) (mean cell-cycle duration for non-confined cells: 14.66 h ± 2.31), regardless of their NE status. In contrast, after a long period (12 h), cells that displayed NE ruptures, while showing no sign of death, did not resume proliferation (Figure 4A, right panel) whereas the few dividing cells showed a much longer cell-cycle duration (Figure 4A). These results suggest that NE rupture and sustained confinement delay cell-cycle progression.

To characterize the senescence phenotype associated with strong confinement, RPE1 cells were confined for short or long periods of time, under weak (4 μm) or strong (2 μm) confinement, then harvested and replated for 96 h before testing a panel of senescence markers (β-gal positivity, heterochromatin foci-HP1γ staining, western blot for lamin B1 and p21) (Gorgoulis et al., 2019). All these markers consistently showed that although short-term or weak (4 μm) confinement did not induce senescence, long-term, strong confinement, induced a robust senescence phenotype in both RPE1 and MCF10A, but not in DCIS cells (Figures 4B–4G and S5E–S5G). TREX1-depleted and TREX1 KO RPE1 cells showed no sign of senescence even after strong and prolonged confinement (Figures 4B, 4C, 4E–4G, and S5E) and expression of TREX1 WT in TREX1 KO cells rescued the induction of p21 by strong confinement in RPE1 cells (Figure 4E). The senescence phenotype was not dependent on the activation of the canonical cGAS pathway (Gorgoulis et al., 2019) because RPE1 cells do not express cGAS (Figure S5H; Basit et al., 2020) and did not show any sign of cGAS enzymatic activity in response to transfected DNA (Figure S5I). Together, these results show that TREX1-dependent chronic DNA damage induced upon strong confinement triggers the hallmarks of the senescence program in normal RPE1 and MCF10A cells but not in transformed DCIS cells.

To investigate the potential consequences of DNA damage associated with NE ruptures during the development of tumors produced by DCIS cells, we used the duct-on-chip assay described above. Both control- and TREX1-depleted cells reached high density within 48 h after injection in the device, showing that proliferation was not affected by TREX1 depletion. They also displayed comparable levels of NE ruptures (Figure 5A, right graph). After 24 h in the device, there was no appreciable difference in 53BP1 foci numbers between control- and TREX1-depleted cells (Figure 5A, left graph). In contrast, although this number significantly increased at 48 h for control cells, it remained constant in TREX1-depleted cells (Figure 5A, left graph). These results indicate that the increased 53BP1 foci levels observed at high density in the duct-on-chip system is a consequence of TREX1-dependent DNA damage following nuclear deformations and ruptures.
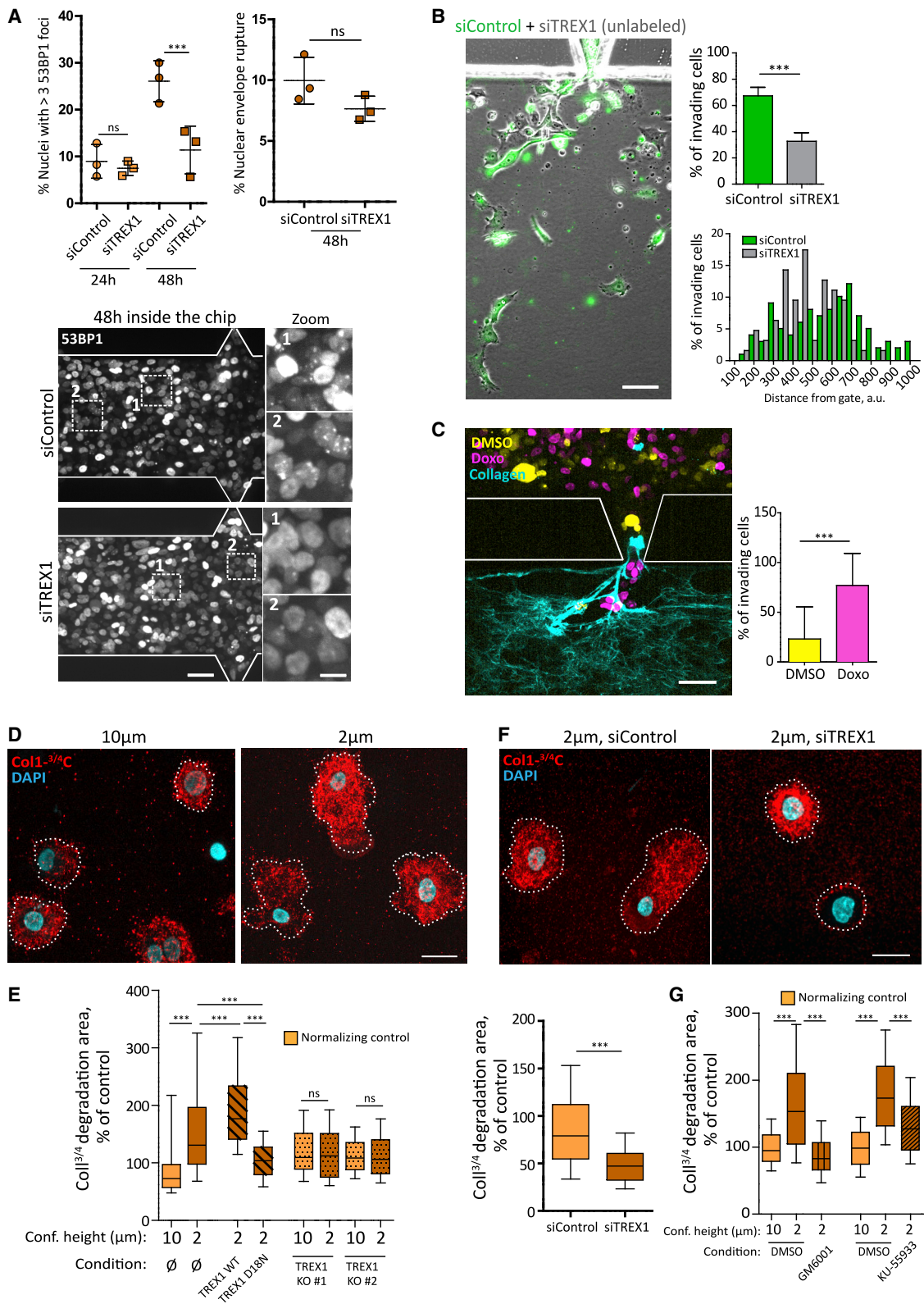
TREX1-depleted DCIS cells can thus grow at high density in the duct-on-chip device without showing an increase in DNA damage. We found that control cells invaded the collagen chamber earlier and migrated farther than TREX1-depleted cells (Figure 5B). This suggests that the increased invasive behavior of control cells might be due to elevated DNA damage. To test this hypothesis, differently labeled control and doxo-treated cells were mixed and injected in the duct-on-chip device. We observed that 24 h after loading the cells into the device (to ensure that cell density was still low), doxo-treated cells displayed increased invasion potential into the collagen chamber as compared to DMSO-treated cells (Figure 5C). These results indicate that sustained DNA damage can be a driver of the invasive behavior of DCIS cells in a 3D matrix environment. We thus assessed the collagen degradation activity of DCIS cells using an antibody that recognizes the collagenase-cleaved $^3/_4$ fragment of collagen I (Castagnino et al., 2018; Infante et al., 2018; Lodillinsky et al., 2016). Cells were either treated with doxo or confined for several hours and then were embedded in a 3D collagen gel in the absence of any further DNA damaging condition. Increasing doses of doxo caused a dose-dependent increase in collagen degradation (Figure S6A), suggesting that prior exposure to DNA damage enhances the collagen degradation capacity of DCIS cells. We then assayed cells after confinement. Once in the collagen gel, the nuclear area of the cells that had been confined at various heights was comparable (Figure S6B), showing no long-lasting nuclear deformation. TREX1-proficient cells that had been confined at 2-μm height, but not TREX1-deficient cells, showed a persistent, highly polarized morphology, increased speed in the collagen network (Figures S6C and quantified in S6D; Video S5) and augmented collagen degradation (Figures 5D–5F). In agreement,

---

(D) Cells were confined for 3 or 12 h at 4 or 2 μm; cells were then harvested and replated for 72 h before lysis for western blot; tubulin is the loading control.

(E) RPE1 TREX1 KO cells or RPE1 TREX1 KO cells reconstituted with TREX1 WT-mCherry were confined at the indicated heights for 12 h. Cells were then harvested, replated, and cultured 72 h before lysis for western blot; tubulin is the loading control. Western blots are representative of 2 independent experiments.

Bars, 80 μm (B) and 10 μm (F). p values were calculated by unpaired Student's t test (A) or one-way ANOVA with post hoc Tukey test (C and G). ***p < 0.0001; **p < 0.005; ns, not significant.

See also Figure S5.

A

% Nuclei with > 3 53BP1 foci

ns   ***

siControl siTREX1 siControl siTREX1

24h   48h

% Nuclear envelope rupture

ns

siControl siTREX1

48h

48h inside the chip   Zoom

53BP1

siControl

siTREX1

1

2

B siControl + siTREX1 (unlabeled)

% of invading cells

***

siControl siTREX1

% of invading cells

siControl
siTREX1

Distance from gate, a.u.

C DMSO Doxo Collagen

% of invading cells

***

DMSO Doxo

D 10μm   2μm

Col1-³/⁴C
DAPI

F 2μm, siControl   2μm, siTREX1

Col1-³/⁴C
DAPI

E

ColI³/⁴ degradation area, % of control

*** *** *** ***

Normalizing control

ns   ns

Conf. height (μm): 10 2 2 2 10 2 10 2

Condition: Ø Ø TREX1 WT TREX1 D18N TREX1 KO #1 TREX1 KO #2

ColI³/⁴ degradation area, % of control

***

siControl siTREX1

G

ColI³/⁴ degradation area, % of control

Normalizing control

*** ***   *** ***

Conf. height (μm): 10 2 2 10 2 2

Condition: DMSO GM6001 DMSO KU-55933

(legend on next page)

overexpressing TREX1-WT augmented collagen degradation whereas TREX1-D18N did not (Figure 5E). Doxo treatment induced collagen degradation in TREX1-depleted cells (Figure S6E), confirming that TREX1 acts upstream of DNA damage to induce collagen degradation. Taken together, these experiments show that, upon strong confinement, TREX1-dependent DNA damage leads to an increase in collagen degradation by DCIS cells.

To further clarify how TREX1-mediated DNA damage induces collagen degradation, cells confined at 2-μm height were treated with the MMP inhibitor, GM6001, or with the ATM inhibitor KU-55933. Both treatments inhibited collagen degradation (Figure 5G). DNA damage during interphase might lead to cGAS activation and the establishment of an EMT-like phenotype (Harding et al., 2017). cGAS-depletion showed that, similarly to the senescence phenotype in RPE1 cells, the induction of collagen degradation upon confinement was not cGAS-dependent (Figure S6F). Increased cellular motility and invasion induced by prolonged DNA damage and ATM activation has been shown to promote a partial EMT state (Peng et al., 2019; Sun et al., 2012). We analyzed the mRNA expression level of a series of canonical EMT genes in cells confined at 10 μm (control) or 2 μm, comparing WT and TREX1 KO cells. We found that SNAIL1 mRNA was specifically upregulated by confinement at 2 μm, and such induction did not occur in two independent TREX1 KO clones (Figure S6G). In the absence of confinement, SNAIL1 was also induced by both doxo and etoposide with a peak at 4 h of treatment (Figure S6H). Moreover, SNAIL1 silencing abrogated the increase in collagen degradation promoted upon strong confinement (Figure S6I). Together, these results suggest that a partial EMT phenotype, including increased matrix degradation and invasive potential, is induced in DCIS cells due to prolonged/chronic exposure to DNA damage.

Putting these results in the context of our initial observations of nuclear deformation and DNA damage both in human breast ductal carcinoma and intraductal DCIS cell tumor xenografts (Figure 1), we hypothesized that TREX1 is responsible for DNA damage in these deformed nuclei, favoring a collagen degradation program, ultimately promoting the *in situ*-to-invasive carcinoma transition. To directly test this hypothesis in an *in vivo* murine model, we injected either parental or TREX1 KO DCIS cells inside the mammary ducts of immuno-suppressed mice and allowed tumors to develop for 6–8 weeks. Both parental- and TREX1 KO-injected mice formed intraductal *in situ* tumors at a similar rate (Figure S6J). However, there was a sharp decrease in the tumor area of TREX1 KO-injected mice compared to parental-injected mice (Figures S6K and S6L). Strikingly, although all the mice injected with parental DCIS cells showed invasive tumors based on whole-mount carmine and histological staining within 6 weeks after injection, the formation of invasive tumors in TREX1 KO-injected mice was greatly reduced for up to 8 weeks (Figures 6A and 6B). This phenotype was comparable to the reduced invasive potential of membrane type I (MT1)-MMP (MMP14)-deficient DCIS cells that we previously reported using this model (Lodillinsky et al., 2016). The proliferation rates of parental DCIS and TREX1 KO clones were similar *in vitro* (Figure S6M). Additionally, analysis of parental and TREX1 KO tumor xenografts revealed no differences in the fraction of cells positive for the proliferation marker Ki67 (Figure 6C). Parental tumors displayed a significantly larger percentage of γH2AX-positive nuclei than TREX1 KO tumors (Figures 6C and 6D). The fraction of cells with high and very high *Z* scores (γH2AX intensity) was enriched at the tumor edge, and this was reduced in TREX1 KO tumors, but not in the tumor bulk (Figures 6E, 6F, and S6N). Overall, these results suggest that the transition from *in situ* to the invasive stage is favored in WT cells by TREX1-dependent DNA damage occurring in deformed and ruptured nuclei as the tumor grows in the confined environment of the mammary ducts.

We also asked whether NE ruptures can be seen in the mice xenograft and in the human tumor. We first used a combination of lamin A/C, γH2AX, and DAPI staining and looked for chromatin herniations (i.e., interruptions of the lamin A/C staining with a protrusion of chromatin labeled by DAPI). We were able to find several of such instances in the intraductal tumor xenografts (Figure 7A), which correlated with nuclei positive for γH2AX staining. Next, we used a combination of cGAS, γH2AX, and DAPI staining. In mouse xenografts, we found regions enriched

Figure 5. TREX1-dependent DNA damage leads to collagen degradation and invasion

(A–C) Duct-on-chip assay. (A) DCIS cells stably expressing 53BP1 and catalytically inactive cGAS were transiently depleted for TREX1 and 48 h later injected in the chip device. Graphs: data represent the mean ± SD of 3 independent experiments where 5 random fields (at 20× magnification) were scored per condition per experiment. Bar, 50 μm; zoom bar, 10 μm. (B) DCIS cells were transiently depleted for TREX1 and 48 h later injected in the same chip device with siControl cells (labeled with a green cell tracker). Graphs: (top) data represent the mean ± SD of 4 independent experiments where cells invading from 7 random gates were scored per experiment; (bottom) frequency distribution histogram of the data displayed on the bar graph. Bar, 50 μm. (C) DCIS cells stably expressing 53BP1-EGFP were pre-treated for 12 h with doxorubicin (Doxo, 20 nM) and co-injected with DCIS cells stably expressing 53BP1-mCherry pre-treated for 12 h with DMSO. Data represent the mean ± SD of 2 independent experiments where cells invading from 10 random gates were scored per experiment. Bar, 40 μm.

(D) DCIS cells were confined for 2 h at the indicated heights. Following the confinement period, cells were harvested and embedded in 3D type I collagen for 12 h. Degraded collagen (red); DAPI (cyan).

(E) A variety of TREX1-deficient or -proficient DCIS cells was confined at the indicated heights. Data represent 3 independent experiments where 50 cells per condition per experiment were analyzed.

(F) TREX1-depleted DCIS cells were confined for 2 h at the indicated heights. Data represent 3 independent experiments where 60 cells per condition per experiment were analyzed. Data were normalized by the mean of control samples.

(G) DCIS cells were confined for 2 h at the indicated heights in the presence of DMSO (vehicle), ATM inhibitor (KU-55933, 10 μM) or MMP inhibitor (GM6001, 40 μM) and then embedded in a 3D collagen gel (still in the presence of the inhibitors). Data represent 3 independent experiments where 60 cells per condition per experiment were analyzed. All box and whisker plots show the median value and 10–90 percentiles of the collagen degradation area.

p values were calculated by unpaired Student's t test (F), χ^2 test (A, right, B, and C), or one-way ANOVA with post hoc Tukey test (E and G). ***p < 0.0001; ns, not significant.
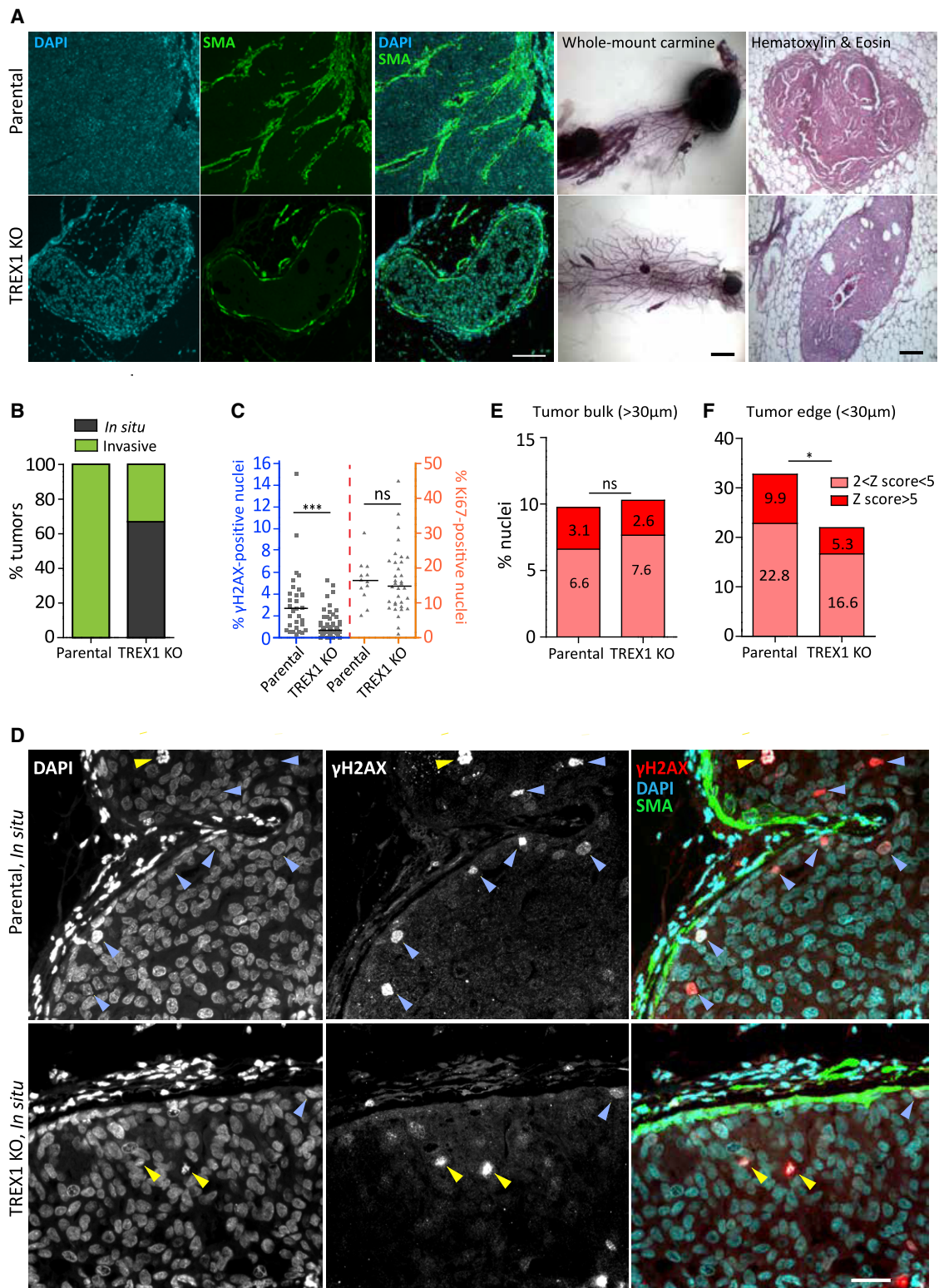
See also Figure S6 and Video S5.

Figure 6. TREX1-dependent DNA damage promotes tumor invasion in mouse xenograft model of breast cancer

(A) Left: immunofluorescence analysis of alpha-smooth muscle actin, SMA (green) and DAPI (cyan) in 6- to 8-week-old mouse xenografts generated by intraductal injection of either parental DCIS cells or DCIS TREX1 KO clones. Bar, 100 μm. Middle: whole-mount carmine-stained 7-week-old glands. Bar, 1 mm. Right: H&E-stained 7-week-old glands. Bar, 60 μm.

(legend continued on next page)

with the typical cGAS perinuclear accumulation that we observed *in vitro*, corresponding to γH2AX-positive nuclei (Figure 7B). Immunohistochemistry provided even clearer examples of NE ruptures, with cGAS staining at the periphery of nuclei (Figure 7C). Of note, the cGAS antibody was validated *in vitro* on DCIS cells depleted for cGAS (Figure S7A). Human breast cancer samples displayed heterogenous cGAS-labeling and cGAS-positive micro-nuclei, but we could also detect numerous NE rupture events (Figure S7B). A complete proof of the role of NE ruptures and TREX1 in human breast tumors will require deeper investigation of a larger number of patient samples. These observations show that NE rupture events occur *in vivo*, both in DCIS tumor xenografts and in human tumors. Therefore cGAS staining has the potential to be a powerful tool to visualize the occurrence of NE rupture events in tumor samples.

DISCUSSION

TREX1 is a cytoplasmic exonuclease, mostly found associated with ER membranes (Lee-Kirsch et al., 2007a, 2007b) and shown to protect cells from the accumulation of cytoplasmic DNA, either from viral or endogenous origins (Mazur and Perrino, 2001; Stetson et al., 2008). Although TREX1 has already been proposed to act on nuclear DNA as well (Chowdhury et al., 2006; Maciejowski et al., 2015, 2019), possibly in conjunction with an endonuclease (Chowdhury et al., 2006) to generate DSBs, so far there is no clear mechanism explaining how TREX1 could act on nuclear chromatin. ROS and irradiation have been shown to induce TREX1 nuclear translocation, although the precise mechanisms remain elusive (Chowdhury et al., 2006; Martinvalet et al., 2005; Yang et al., 2007). Based on our imaging and rescue experiments, we speculate that TREX1 translocation could potentially occur upon fusion of the outer and inner nuclear membranes following NE ruptures. This could allow ER proteins, by diffusion on the membrane, to gain access to the inner nuclear membrane and potentially to the poorly characterized intranuclear membrane networks of the nuclear reticulum (Malhas et al., 2011). It is likely that the whole ER-bound SET complex transfers to the inner nuclear membrane upon NE rupture events. The SET complex has previously been implicated in the induction of TREX1-dependent nuclear DNA double strand breaks (Chowdhury et al., 2006). In agreement, we did not observe any transient formation of single strand breaks upon confinement using RPA-GFP, which displayed DNA damage foci upon treatment with hydroxyurea (Figure S7C). We thus speculate that DNA damage after NE rupture could also implicate other members of the SET complex that, together with the TREX1 exonuclease, gain access to inner nuclear membranes due to fusion of the outer and inner nuclear membranes at sites of rupture.

In the model systems here studied, the DNA damage response pathway is involved both in the senescence phenotype in RPE1 cells and in the induction of the collagenolytic response in the senescence-deficient DCIS cell line. This is in contrast to the cGAS-dependent inflammatory pathway (Liu et al., 2018)(Harding et al., 2017), which does not seem to be required in our experiments. A potential effect of ATM activation by DNA damage is a cell-cycle arrest. We indeed found that doxo-treated DCIS cells showed a reduction of cells in S/G2 upon 48 h of treatment (Figure S7D). Nevertheless, this cell-cycle arrest per se does not explain the increase in collagen degradation because this response was not increased comparing cells in G1 versus S/G2 (Figure S7E). Two recent studies pointed to a potential activation of an EMT-like phenotype downstream of ATM activation (Jiang et al., 2019; Peng et al., 2019). Furthermore, several ATM substrates have also been associated with lysosomal activity and thus potentially to collagen degradation (Kang et al., 2017). Our results suggest that upon chronic, sub-lethal levels of DNA damage, cells that have lost the normal ATM-dependent senescence-associated proliferation arrest could initiate a partial EMT program including an invasive behavior, driving the transition from *in situ* to invasive carcinoma stages.

A recent study (Shah et al., 2021) found that DNA damage can be triggered by confinement independently of NE rupture events in some cell lines, including MDA-MB-231 cells. We thus assayed these cells and found that DNA damage upon confinement was both NE rupture- and TREX1-independent (Figures S7G and S7H). These results suggest that tumors might be differentially sensitive to TREX1 inhibition.

Our experiments do not prove that TREX1 is the main driver of DNA damage in the human disease nor that DNA damage associated with nuclear deformation plays a role in the human disease progression. TREX1 has been described to promote pro- or anti-tumoral effects depending on different cellular and tumoral contexts (Benci et al., 2019; Erdal et al., 2017; Vanpouille-Box et al., 2017). To get further insight into this question, we analyzed the association of TREX1 expression levels in breast cancer with overall survival using public datasets. This analysis revealed that high level of TREX1 expression is significantly associated with reduced probability of survival (Figure S7F). Thus, targeting this exonuclease might be an effective therapeutic strategy to curb tumor progression, while promoting

(B) Classification of the tumor xenograft stage 6–8 weeks post-intraductal injection of either parental DCIS cells or DCIS TREX1 KO clones from 3 independent mice injections. Data represent a total of 7 glands scored for DCIS parental tumors and 14 glands for TREX1 KO tumors (TREX1 KO #1 + TREX1 KO #2 clones).
(C) Scatter dot plots of γH2AX- and Ki67-positive nuclei (lines are median) 6–8 weeks post-intraductal injection. A total of 13 parental and 34 TREX1 KO (18 TREX1 KO #1 + 16 TREX1 KO #2) images were analyzed for Ki67 scoring; a total of 31 parental and 62 TREX1 KO (35 TREX1 KO #1 + 27 TREX1 KO #2) images were analyzed for γH2AX scoring.
(D) Immunofluorescence analysis of γH2AX (red), alpha-smooth muscle actin, SMA (green), and DAPI (cyan) in 6- to 8-week-old mouse xenografts generated by intraductal injection of either parental DCIS cells or DCIS TREX1 KO clones. Blue arrowheads point to DNA damage-γH2AX-positive cells; yellow arrowheads point to mitotic or apoptotic figures. Bar, 40 μm.
(E and F) Z score categories (γH2AX intensities, see STAR Methods and Figure S1A) of nuclei localized in the tumor bulk (E) or in the tumor edge (determined by the myoepithelial layer) (F). Data represent a total of 23 images analyzed for DCIS parental tumors and 30 images for DCIS TREX1 KO tumors from 3 independent mice injections. p values were calculated by unpaired Student's t test, ***p < 0.0001; *p < 0.05; ns, not significant.
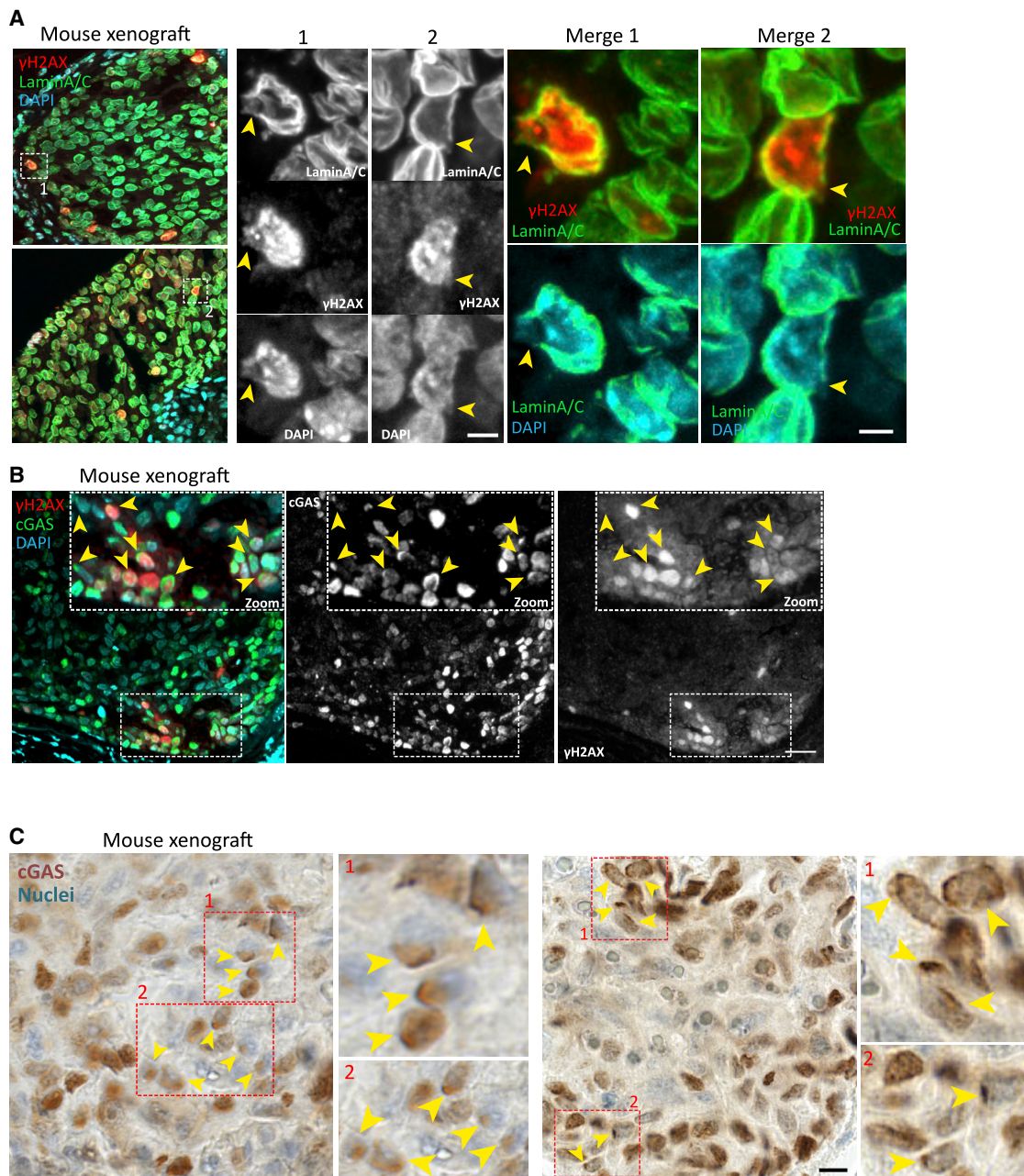See also Figure S6.

Figure 7. Mouse tumor xenografts display NE rupture and DNA damage

(A) Immunofluorescence analysis of lamin A/C (green), DAPI (cyan), and γH2AX (red). Bar, 25 μm; inset bars, 5 μm (single channels) and 3 μm (merged channels).

(B) Multiplex immunofluorescence analysis of cGAS (green), DAPI (cyan), and γH2AX (red). Bar, 60 μm.

(C) cGAS immunohistochemistry (brown) and nuclei (blue). Bar, 25 μm. All analysis was performed in mouse xenografts at *in situ*-advanced stage generated by intraductal injection of parental DCIS cells. Yellow arrowheads point to NE rupture events.

See also Figure S7.

anti-tumoral immune response via cGAS activation (Stetson et al., 2008; Takahashi et al., 2018).

In this study, we focused on mammary tumors, but NE ruptures could also occur in other tumors. As a proof of concept, we performed cGAS staining on colorectal tumor samples. In 2 patients out of 4 tested, we observed a good correlation between regions highly enriched in nuclei positive for γH2AX, which corresponded to the invasive front of the tumor, and regions with a high fraction of nuclei with NE rupture events (Figures S7I–S7K). A broader study is needed to assess whether our findings can be extended to other tumor types.

We and others have shown that the NE is a fragile barrier constantly being challenged in physiology and disease (Denais et al., 2016; Raab et al., 2016; Srivastava et al., 2021; Nader, 2021). The occurrence of DNA damage associated with nuclear deformations is likely to be a common phenomenon. In normal tissues, this would trigger cellular senescence, contributing to developmental programs and tissue homeostasis, or even participating in tissue aging. In contrast, in tumor cells, in which the senescence checkpoint has been lost, it would lead to an aberrant invasiveness in the absence of a proliferative arrest, promoting tumor growth and invasion.

Limitations of the study

Double labeling with fluorescent 53BP1 and icGAS in live cells unambiguously demonstrated the causal relationship between NE rupture events and DNA damage. However, the different dynamics of icGAS entry and exit from the nucleus and DNA damage foci appearance and repair generate a more complex set of situations when considering cells at a fixed time point or fixed cells stained with these two proteins by immunofluorescence. This difficulty is exacerbated in 3D samples in which NE rupture events can happen out of the plan of imaging. In cases in which a direct live observation of the rupture events is difficult (e.g., in slices of tumor samples or in the duct on chip assay), cells in which cGAS perinuclear accumulation and DNA damage are simultaneously present likely represent only a subset of the cells that have undergone NE rupture-dependent DNA damage, making precise quantification difficult.

STAR★METHODS

Detailed methods are provided in the online version of this paper and include the following:

- ● KEY RESOURCES TABLE
- ● RESOURCE AVAILABILITY
  - ○ Lead contact
  - ○ Materials availability
  - ○ Data and code availability
- ● EXPERIMENTAL MODEL AND SUBJECT DETAILS
  - ○ Mice
  - ○ Intraductal transplantation method
  - ○ Human tissues
  - ○ Human Cell lines
- ● METHOD DETAILS
  - ○ Constructs
  - ○ Lentiviral particles production in 293FT cells and Lentivector transductions
  - ○ Quantitative RT-PCR analysis
  - ○ cGAMP extraction with methanol/water
  - ○ Generation of TREX1 CRISPR clones
  - ○ Duct-on-a-chip assay
  - ○ Human primary tumor samples
  - ○ Immunohistochemistry and spectral multiplex (processed using Bond RX automated-Leica)
  - ○ Histological and immunofluorescence analysis of mouse tissue sections
  - ○ Indirect immunofluorescence microscopy

- ○ 3D type I collagen degradation assay
- ○ Transfection procedure and siRNA oligonucleotides
- ○ Drug treatments
- ○ Western blotting
- ○ Microfabrication-based confinement
- ○ Live-cell imaging
- ○ Measurements of γH2AX intensity relative to tumor edge in mice xenografts
- ○ Electron microscopy
- ● QUANTIFICATION AND STATISTICAL ANALYSIS

AUTHOR CONTRIBUTIONS

G.P.d.F.N. designed and performed the experiments, analyzed and interpreted the data, and wrote the manuscript. S.A.-G. and G.P.d.F.N. performed the 3D collagen degradation assays. S.A.-G., A.Y., C.V., P.C., and J.-L.V.

designed the duct-on-chip device. F.R. and E.L. performed the mouse xeno-graft assays and S.A.-G., F.R., and G.P.d.F.N. analyzed the data. M. Gratia performed the sequencing of the TREX1 CRISPR clones and generated some stable cell lines. M.M. wrote ImageJ macros for data analysis and helped on data interpretation. A.W. performed and quantified the experiments with DCIS cells expressing geminin-mCherry. R.N.R. and J.G. designed and per-formed multiplex IF and IHC on mice xenografts samples and IHC on human tumor samples. A.P. performed the quantitative RT-PCR analysis. C.C. analyzed data relative to the cell division cycle. M. Gentili generated stable cell lines and performed molecular cloning. C.L. provided images of mouse xe-nografts for analysis. V.C. and C.T. performed and interpreted the assays involving human primary tumors. G.S. designed, supervised, and interpreted the assays involving human primary tumors and edited the manuscript. P.C. designed, supervised, and interpreted the mouse xenograft assays and edited the manuscript. N.M. conceptualized the role of TREX1, helped design and interpret experiments, supervised M. Gratia, and edited the manuscript. G.P.d.F.N., S.A.-G., M.P., P.C., N.M., and G.S. actively engaged in discus-sions throughout the study. M.P. supervised the study, designed the experi-ments, interpreted the data, and wrote the manuscript.

REFERENCES

Basit, A., Cho, M.G., Kim, E.Y., Kwon, D., Kang, S.J., and Lee, J.H. (2020). The cGAS/STING/TBK1/IRF3 innate immunity pathway maintains chromosomal stability through regulation of p21 levels. Exp. Mol. Med. *52*, 643–657.

Behbod, F., Kittrell, F.S., LaMarca, H., Edwards, D., Kerbawy, S., Heestand, J.C., Young, E., Mukhopadhyay, P., Yeh, H.W., Allred, D.C., et al. (2009). An intraductal human-in-mouse transplantation model mimics the subtypes of ductal carcinoma in situ. Breast Cancer Res. *11*, R66.

Benci, J.L., Johnson, L.R., Choa, R., Xu, Y., Qiu, J., Zhou, Z., Xu, B., Ye, D., Nathanson, K.L., June, C.H., et al. (2019). Opposing Functions of Interferon Coordinate Adaptive and Innate Immune Responses to Cancer Immune Checkpoint Blockade. Cell *178*, 933–948.e14.

Blaha, L., Zhang, C., Cabodi, M., and Wong, J.Y. (2017). A microfluidic plat-form for modeling metastatic cancer cell matrix invasion. Biofabrication *9*, 045001.

Castagnino, A., Castro-Castro, A., Irondelle, M., Guichard, A., Lodillinsky, C., Fuhrmann, L., Vacher, S., Agüera-González, S., Zagryazhskaya-Masson, A., Romao, M., et al. (2018). Coronin 1C promotes triple-negative breast cancer invasiveness through regulation of MT1-MMP traffic and invadopodia function. Oncogene *37*, 6425–6441.

Cho, S., Vashisth, M., Abbas, A., Majkut, S., Vogel, K., Xia, Y., Ivanovska, I.L., Irianto, J., Tewari, M., Zhu, K., et al. (2019). Mechanosensing by the lamina protects against nuclear rupture, DNA damage, and cell-cycle arrest. Dev. Cell *49*, v920–935.e5.

Chowdhury, D., Beresford, P.J., Zhu, P., Zhang, D., Sung, J.S., Demple, B., Perrino, F.W., and Lieberman, J. (2006). The exonuclease TREX1 is in the SET complex and acts in concert with NM23-H1 to degrade DNA during gran-zyme A-mediated cell death. Mol. Cell *23*, 133–142.

De Vos, W.H., Houben, F., Kamps, M., Malhas, A., Verheyen, F., Cox, J., Man-ders, E.M.M., Verstraeten, V.L.R.M., Van steensel, M.A.M., Marcelis, C.L.M., et al. (2011). Repetitive disruptions of the nuclear envelope invoke temporary loss of cellular compartmentalization in laminopathies. Hum. Mol. Genet. *20*, 4175–4186.

Denais, C.M., Gilbert, R.M., Isermann, P., McGregor, A.L., te Lindert, M., Wei-gelin, B., Davidson, P.M., Friedl, P., Wolf, K., and Lammerding, J. (2016). Nu-clear envelope rupture and repair during cancer cell migration. Science *352*, 353–358.

Earle, A.J., Kirby, T.J., Fedorchak, G.R., Isermann, P., Patel, J., Iruvanti, S., Moore, S.A., Bonne, G., Wallrath, L.L., and Lammerding, J. (2020). Mutant lam-ins cause nuclear envelope rupture and DNA damage in skeletal muscle cells. Nat. Mater. *19*, 464–473.

Erdal, E., Haider, S., Rehwinkel, J., Harris, A.L., and McHugh, P.J. (2017). A prosurvival DNA damage-induced cytoplasmic interferon response is medi-ated by end resection factors and is limited by Trex1. Genes Dev. *31*, 353–369.

Feinberg, T.Y., Zheng, H., Liu, R., Wicha, M.S., Yu, S.M., and Weiss, S.J. (2018). Divergent Matrix-Remodeling Strategies Distinguish Developmental from Neoplastic Mammary Epithelial Cell Invasion Programs. Dev. Cell *47*, 145–160.e6.

Feng, C., Yang, M., Zhang, Y., Lan, M., Huang, B., Liu, H., and Zhou, Y. (2018). Cyclic mechanical tension reinforces DNA damage and activates the p53-p21-Rb pathway to induce premature senescence of nucleus pulposus cells. Int. J. Mol. Med. *41*, 3316–3326.

Friedl, P., and Gilmour, D. (2009). Collective cell migration in morphogenesis, regeneration and cancer. Nat. Rev. Mol. Cell Biol. *10*, 445–457.

Gentili, M., Lahaye, X., Nadalin, F., Nader, G.P.F., Lombardi, E.P., Herve, S., De Silva, N.S., Rookhuizen, D.C., Zueva, E., Goudot, C., et al. (2019). The N-Terminal Domain of cGAS Determines Preferential Association with Centro-meric DNA and Innate Immune Activation in the Nucleus. Cell Rep. *26*, 2377–2393.e13.

Gorgoulis, V., Adams, P.D., Alimonti, A., Bennett, D.C., Bischof, O., Bishop, C., Campisi, J., Collado, M., Evangelou, K., Ferbeyre, G., et al. (2019). Cellular Senescence: Defining a Path Forward. Cell *179*, 813–827.

Harding, S.M., Benci, J.L., Irianto, J., Discher, D.E., Minn, A.J., and Greenberg, R.A. (2017). Mitotic progression following DNA damage enables pattern recog-nition within micronuclei. Nature *548*, 466–470.

Hatch, E.M. (2018). Nuclear envelope rupture: little holes, big openings. Curr. Opin. Cell Biol. *52*, 66–72.

Hatch, E.M., and Hetzer, M.W. (2016). Nuclear envelope rupture is induced by actin-based nucleus confinement. J. Cell Biol. *215*, 27–36.

Infante, E., Castagnino, A., Ferrari, R., Monteiro, P., Agüera-González, S., Paul-Gilloteaux, P., Domingues, M.J., Maiuri, P., Raab, M., Shanahan, C.M., et al. (2018). LINC complex-Lis1 interplay controls MT1-MMP matrix digest-on-demand response for confined tumor cell migration. Nat. Commun. *9*, 2443.

Irianto, J., Xia, Y., Pfeifer, C.R., Athirasala, A., Ji, J., Alvey, C., Tewari, M., Ben-nett, R.R., Harding, S.M., Liu, A.J., et al. (2017). DNA Damage Follows Repair Factor Depletion and Portends Genome Variation in Cancer Cells after Pore Migration. Curr. Biol. *27*, 210–223.

Jiang, Y.N., Ni, X.Y., Yan, H.Q., Shi, L., Lu, N.N., Wang, Y.N., Li, Q., and Gao, F.G. (2019). Interleukin 6-triggered ataxia-telangiectasia mutated kinase acti-vation facilitates epithelial-to-mesenchymal transition in lung cancer by upre-gulating vimentin expression. Exp. Cell Res. *381*, 165–171.

Kang, H.T., Park, J.T., Choi, K., Kim, Y., Choi, H.J.C., Jung, C.W., Lee, Y.S., and Park, S.C. (2017). Chemical screening identifies ATM as a target for alle-viating senescence. Nat. Chem. Biol. *13*, 616–623.

Kim, M., Kim, H.J., Chung, Y.R., Kang, E., Kim, E.K., Kim, S.H., Kim, Y.J., Kim, J.H., Kim, I.A., and Park, S.Y. (2018). Microinvasive carcinoma versus ductal carcinoma in situ: A comparison of clinicopathological features and clinical outcomes. J. Breast Cancer *21*, 197–205.

Lahaye, X., Satoh, T., Gentili, M., Cerboni, S., Conrad, C., Hurbain, I., El Mar-jou, A., Lacabaratz, C., Lelièvre, J.-D., and Manel, N. (2013). The capsids of HIV-1 and HIV-2 determine immune detection of the viral cDNA by the innate sensor cGAS in dendritic cells. Immunity *39*, 1132–1142.

Le Berre, M., Aubertin, J., and Piel, M. (2012). Fine control of nuclear confine-ment identifies a threshold deformation leading to lamina rupture and induc-tion of specific genes. Integr. Biol. *4*, 1406–1414.

Le Berre, M., Zlotek-Zlotkiewicz, E., Bonazzi, D., Lautenschlaeger, F., and Piel, M. (2014). Methods for Two-Dimensional Cell Confinement. Methods Cell Biol. *121*, 213–229.

Lee-Kirsch, M.A., Chowdhury, D., Harvey, S., Gong, M., Senenko, L., Engel, K., Pfeiffer, C., Hollis, T., Gahr, M., Perrino, F.W., et al. (2007a). A mutation in TREX1 that impairs susceptibility to granzyme A-mediated cell death underlies familial chilblain lupus. J. Mol. Med. (Berl.) *85*, 531–537.

Lee-Kirsch, M.A., Gong, M., Chowdhury, D., Senenko, L., Engel, K., Lee, Y.A., de Silva, U., Bailey, S.L., Witte, T., Vyse, T.J., et al. (2007b). Mutations in the gene encoding the 3′-5′ DNA exonuclease TREX1 are associated with systemic lupus erythematosus. Nat. Genet. *39*, 1065–1067.

Lehtinen, D.A., Harvey, S., Mulcahy, M.J., Hollis, T., and Perrino, F.W. (2008). The TREX1 double-stranded DNA degradation activity is defective in dominant mutations associated with autoimmune disease. J. Biol. Chem. *283*, 31649–31656.

Liu, Y.-J., Le Berre, M., Lautenschlaeger, F., Maiuri, P., Callan-Jones, A., Heuzé, M., Takaki, T., Voituriez, R., and Piel, M. (2015). Confinement and low adhesion induce fast amoeboid migration of slow mesenchymal cells. Cell *160*, 659–672.

Liu, H., Zhang, H., Wu, X., Ma, D., Wu, J., Wang, L., Jiang, Y., Fei, Y., Zhu, C., Tan, R., et al. (2018). Nuclear cGAS suppresses DNA repair and promotes tumorigenesis. Nature *563*, 131–136.

Lodillinsky, C., Infante, E., Guichard, A., Chaligné, R., Fuhrmann, L., Cyrta, J., Irondelle, M., Lagoutte, E., Vacher, S., Bonsang-Kitzis, H., et al. (2016). p63/MT1-MMP axis is required for in situ to invasive transition in basal-like breast cancer. Oncogene *35*, 344–357.

Lusk, C.P., and Ader, N.R. (2020). CHMPions of repair: Emerging perspectives on sensing and repairing the nuclear envelope barrier. Curr. Opin. Cell Biol. *64*, 25–33.

Maciejowski, J., Li, Y., Bosco, N., Campbell, P.J., and de Lange, T. (2015). Chromothripsis and Kataegis Induced by Telomere Crisis. Cell *163*, 1641–1654.

Maciejowski, J., Chatzipli, A., Dananberg, A., de Lange, T., and Campbell, P. (2019). APOBEC3B-dependent kataegis and TREX1-driven chromothripsis in telomere crisis. bioRxiv. https://doi.org/10.1101/725366.

Malhas, A., Goulbourne, C., and Vaux, D.J. (2011). The nucleoplasmic reticulum: form and function. Trends Cell Biol. *21*, 362–373.

Malinverno, C., Corallino, S., Giavazzi, F., Bergert, M., Li, Q., Leoni, M., Disanza, A., Frittoli, E., Oldani, A., Martini, E., et al. (2017). Endocytic reawakening of motility in jammed epithelia. Nat. Mater. *16*, 587–596.

Martinvalet, D., Zhu, P., and Lieberman, J. (2005). Granzyme A induces caspase-independent mitochondrial damage, a required first step for apoptosis. Immunity *22*, 355–370.

Mayhew, T.M. (2011). Mapping the distributions and quantifying the labelling intensities of cell compartments by immunoelectron microscopy: progress towards a coherent set of methods. J. Anat. *219*, 647–660.

Mazur, D.J., and Perrino, F.W. (2001). Excision of 3′ termini by the Trex1 and TREX2 3′→5′ exonucleases. Characterization of the recombinant proteins. J. Biol. Chem. *276*, 17022–17029.

Mohr, L., Toufektchan, E., von Morgen, P., Chu, K., Kapoor, A., and Maciejowski, J. (2021). ER-directed TREX1 limits cGAS activation at micronuclei. Mol. Cell *81*, 724–738.e9.

Nader. (2021). Current Opinion in Cell Biology. https://doi.org/10.1016/j.ceb.2021.01.007.

Palamidessi, A., Malinverno, C., Frittoli, E., Corallino, S., Barbieri, E., Sigismund, S., Beznoussenko, G.V., Martini, E., Garre, M., Ferrara, I., et al.

(2019). Unjamming overcomes kinetic and proliferation arrest in terminally differentiated cells and promotes collective motility of carcinoma. Nat. Mater. *18*, 1252–1263.

Peng, B., Ortega, J., Gu, L., Chang, Z., and Li, G.M. (2019). Phosphorylation of proliferating cell nuclear antigen promotes cancer progression by activating the ATM/Akt/GSK3β/Snail signaling pathway. J. Biol. Chem. *294*, 7037–7045.

Raab, M., Gentili, M., de Belly, H., Thiam, H.-R., Vargas, P., Jimenez, A.J., Lautenschlaeger, F., Voituriez, R., Lennon-Dumenil, A.-M., Manel, N., et al. (2016). ESCRT III repairs nuclear envelope ruptures during cell migration to limit DNA damage and cell death. Science *352*, 359–362.

Robijns, J., Houthaeve, G., Braeckmans, K., and De Vos, W.H. (2018). Loss of Nuclear Envelope Integrity in Aging and Disease. Int. Rev. Cell Mol. Biol *336*, 205–222.

Roman, W., Martins, J.P., Carvalho, F.A., Voituriez, R., Abella, J.V.G., Santos, N.C., Cadot, B., Way, M., and Gomes, E.R. (2017). Myofibril contraction and crosslinking drive nuclear movement to the periphery of skeletal muscle. Nat. Cell Biol. *19*, 1189–1201.

Shah, P., Wolf, K., and Lammerding, J. (2017). Bursting the Bubble - Nuclear Envelope Rupture as a Path to Genomic Instability? Trends Cell Biol. *27*, 546–555.

Shah, P., Hobson, C.M., Cheng, S., Colville, M.J., Paszek, M.J., Superfine, R., and Lammerding, J. (2021). Nuclear Deformation Causes DNA Damage by Increasing Replication Stress. Curr. Biol. *31*, 753–765.e6.

Slot, J.W., and Geuze, H.J. (2007). Cryosectioning and immunolabeling. Nat. Protoc. *2*, 2480–2491.

Srivastava, N., Nader, G.P.F., Williart, A., Rollin, R., Cuvelier, D., Lomakin, A., and Piel, M. (2021). Nuclear fragility, blaming the blebs. Curr. Opin. Cell Biol. *70*, 100–108.

Stetson, D.B., Ko, J.S., Heidmann, T., and Medzhitov, R. (2008). Trex1 Prevents Cell-Intrinsic Initiation of Autoimmunity. Cell *134*, 587–598.

Sun, M., Guo, X., Qian, X., Wang, H., Yang, C., Brinkman, K.L., Serrano-Gonzalez, M., Jope, R.S., Zhou, B., Engler, D.A., et al. (2012). Activation of the ATM-Snail pathway promotes breast cancer metastasis. J. Mol. Cell Biol. *4*, 304–315.

Takahashi, A., Loo, T.M., Okada, R., Kamachi, F., Watanabe, Y., Wakita, M., Watanabe, S., Kawamoto, S., Miyata, K., Barber, G.N., et al. (2018). Downregulation of cytoplasmic DNases is implicated in cytoplasmic DNA accumulation and SASP in senescent cells. Nat. Commun. *9*, 1249.

Teulière, J., Faraldo, M.M., Deugnier, M.A., Shtutman, M., Ben-Ze'ev, A., Thiery, J.P., and Glukhova, M.A. (2005). Targeted activation of beta-catenin signaling in basal mammary epithelial cells affects mammary development and leads to hyperplasia. Development *132*, 267–277.

Ungricht, R., and Kutay, U. (2015). Establishment of NE asymmetry—targeting of membrane proteins to the inner nuclear membrane. Curr. Opin. Cell Biol. *34*, 135–141.

Vanpouille-Box, C., Alard, A., Aryankalayil, M.J., Sarfraz, Y., Diamond, J.M., Schneider, R.J., Inghirami, G., Coleman, C.N., Formenti, S.C., and Demaria, S. (2017). DNA exonuclease Trex1 regulates radiotherapy-induced tumour immunogenicity. Nat. Commun. *8*, 15618.

Vargas, J.D., Hatch, E.M., Anderson, D.J., and Hetzer, M.W. (2012). Transient nuclear envelope rupturing during interphase in human cancer cells. Nucleus *3*, 88–100.

Yang, Y.G., Lindahl, T., and Barnes, D.E. (2007). Trex1 Exonuclease Degrades ssDNA to Prevent Chronic Checkpoint Activation and Autoimmune Disease. Cell *131*, 873–886.

Cell
Article

STAR★METHODS

KEY RESOURCES TABLE

REAGENT or RESOURCE	SOURCE	IDENTIFIER
Antibodies		
Rabbit monoclonal anti-Rab5 (clone EPR5438)	Abcam	Cat# ab109534; RRID: AB_10865740
Rabbit polyclonal anti-gamma H2A.X, phospho Ser139	Abcam	Cat# ab11174; RRID: AB_297813
Rabbit monoclonal anti-Ku70 (clone EPR4026)	Abcam	Cat# ab108604; RRID: AB_10861861
Rabbit monoclonal anti-p21 (clone ERF3993)	Abcam	Cat# ab109199; RRID: AB_10861551
Mouse monoclonal anti-Ki67 (clone MIB-1)	Agilent	Cat# M7240; RRID: AB_2142367
Mouse monoclonal anti-alpha SMA (clone 1A4)	Agilent	Cat# M0851; RRID: AB_2223500
Rabbit polyclonal anti-RIF1	Bethyl Laboratories	Cat# A300-569A; RRID: AB_669804
Rabbit monoclonal anti-cGAS (clone D1D3G)	Cell Signaling Technology	Cat# 15102; RRID: AB_2732795
Rabbit monoclonal anti-TREX1 (clone D8E2O) (discontinued)	Cell Signaling Technology	Cat# 15107; RRID: AB_2798710
Rabbit monoclonal anti-GAPDH (clone 14C10)	Cell Signaling Technology	Cat# 2118, RRID: AB_561053
Rabbit monoclonal anti-Snail1 (clone C15D3)	Cell Signaling Technology	Cat# 3879, RRID: AB_2255011
Mouse monoclonal anti-PDI (clone 1D3)	Enzo LifeSciences	Cat# ADI-SPA-891, RRID: AB_10615355
Rabbit polyclonal anti-mCherry	GeneTex	Cat# GTX128508; RRID: AB_2721247
Rabbit polyclonal anti-Col1-3/4C (collagenase-cleaved 3/4 fragment of collagen I)	ImmunoGlobe GmbH	Cat# #0217-050; RRID: AB_2893279
Mouse monoclonal anti-phospho-Histone H2A.X (Ser139) (clone JBW301)	Millipore	Cat# 05-636; RRID: AB_309864
Mouse monoclonal anti-HP1γ (clone 14D3.1)	Millipore	Cat# MABE656; RRID: AB_2722628
Mouse monoclonal anti-TREX1 (clone E-6)	Santa Cruz Biotechnology	Cat# sc-271870; RRID: AB_10708266
Mouse monoclonal anti-laminB1 (clone A-11)	Santa Cruz Biotechonology	Cat# sc-377000, RRID: AB_2861346
Mouse monoclonal anti-αtubulin (clone DM1A)	Sigma-Aldrich	Cat# T9026; RRID: AB_477593
Biological samples		
Human Breast Ductal Adenocarcinoma tissue sections	Archival anonymized tumor tissue collection; Tumor Immunology Unit, Department of Health Sciences, University of Palermo School of Medicine	claudio.tripodo@unipa.it
Chemicals, peptides, and recombinant proteins		
KU-55933 (ATM kinase inhibitor)	Abcam	Cat# 120637; CAS: 587871-26-9
Unlabeled type I collagen	BD Biosciences	Cat# 354236
Etoposide	Cell Signaling Technology	Cat# 2200; CAS: 33419-42-0
Doxorubicin	Cell Signaling Technology	Cat# 5927; CAS: 25316-40-9
Penicillin Streptomycin	GIBCO	Cat# 15140-122
Unlabeled type I collagen, 5mg/ml	IBIDI	Cat# 50201

(Continued on next page)

Continued

REAGENT or RESOURCE	SOURCE	IDENTIFIER
GM6001 (matrix metalloproteinases pan-inhibitor)	Millipore	Cat# CC1010
Human EGF	Peprotech	Cat# AF-100-15; CAS: 62253-63-8
Hydrocortisone	Sigma-Aldrich	Cat# H0888; CAS: 50-23-7
Cholera toxin	Sigma-Aldrich	Cat# C8052; CAS: 9012-63-9
Insulin	Sigma-Aldrich	Cat# I9278; CAS: 11061-68-0
HT-DNA – Deoxyribonucleic acid sodium salt from herring testes	Sigma-Aldrich	Cat# D6898 ; CAS: 438545-06-3
Matrigel	Sigma-Aldrich	Cat# E1270
Protein A gold conjugates	Utrecht University, the Netherlands	N/A
Harris's Hematoxylin	Bio-Optica	Cat# 05-06004/L
pLL-g-PEG	SuSoS	Cat# PLL(20)-g[3.5]-PEG(2)
Critical commercial assays		
2′3′-cGAMP ELISA kit	Interchim	Cat# 501700
DAB Chromogen Kit	BioCare Medical	Cat# DB801L
Vulcan fast red Chromogen Kit	BioCare Medical	Cat# FR805M
Opal 7-Color IHC Kit	Akoya 23 Biosciences	Cat# NEL821001KT
Experimental models: Cell lines		
Human, female: RPE1	Lab of Dr. Matthieu Piel, Institut Curie, Paris	Originally ATCC CRL-4000
Human, female: RPE1 stably expressing icGAS-GFP	This paper	N/A
Human, female: RPE1 stably expressing icGAS-mcherry and 53BP1-GFP	This paper	N/A
Human, female: RPE1 TREX1 KO	This paper	N/A
Human, female: RPE1 TREX1 KO stably expressing icGAS-mcherry and 53BP1-GFP	This paper	N/A
Human, female: MCF10A	Lab of Dr. Philippe Chavrier, Institut Curie, Paris	Originally ATCC CRL-10317
Human, female: MCF10A stably expressing icGAS-mcherry and 53BP1-GFP	This paper	N/A
Human, female: MCF10DCIS.com	Lab of Dr. Philippe Chavrier, Institut Curie, Paris; Behbod et al., 2009	Originally from Asterand (Detroit, MI, USA)
Human, female: MCF10DCIS.com stably expressing icGAS-mcherry and 53BP1-GFP	This paper	N/A
Human, female: MCF10DCIS.com TREX1 KO	This paper	N/A
Human, female: MCF10DCIS.com TREX1 KO stably expressing icGAS-mcherry and 53BP1-GFP	This paper	N/A
Human, female: MDA-MB-231	Lab of Dr. Philippe Chavrier, Institut Curie, Paris	Originally ATCC CRM-HTB-26
Human, female: MDA-MB-231 stably expressing icGAS-mcherry and 53BP1-GFP	This paper	N/A
Experimental models: Organisms/strains		
Mouse: CB17/Icr-Prkdc^scid^/IcrIcoCrl	Charles River Laboratories	Strain code #236
Oligonucleotides		
ON-TARGETplus SMARTpool siTREX1	Dharmacon	Cat# L-013239-02-0005

(Continued on next page)

Continued

REAGENT or RESOURCE	SOURCE	IDENTIFIER
ON-TARGETplus SMARTpool sicGAS (MB21D1)	Dharmacon	Cat# L-015607-02-0005
ON-TARGETplus SMARTpool siSNAI1	Dharmacon	Cat# L-010847-01-0005
TREX1 guide RNA to generate CRISPR KO clones: 5′-GAGCCCCCCCCACCT CTC-(PAM)-3′	Maciejowski et al., 2015	Lab of Titia De Lange, Rockefeller University, New York, USA
GAPDH: NM_001289746.1 (sequence copyright protected)	This paper	Thermo Fischer
CDH2: NM_001308176.1 (sequence copyright protected)	This paper	Thermo Fischer
VIM: NM_003380.3 (sequence copyright protected)	This paper	Thermo Fischer
SNAI1: NM_005985.3 (sequence copyright protected)	This paper	Thermo Fischer
SNAI2: NM_003068.4 (sequence copyright protected)	This paper	Thermo Fischer
TWIST1: NM_000474.3 (sequence copyright protected)	This paper	Thermo Fischer
ZEB1: NM_001128128.2 (sequence copyright protected)	This paper	Thermo Fischer
Recombinant DNA		
pTRIP-CMV-mCherry-TREX1 WT	Lab of Dr. Nicolas Manel, Institut Curie, Paris	N/A
pTRIP-CMV-mCherry-TREX1 D18N	Lab of Dr. Nicolas Manel, Institut Curie, Paris	N/A
pLENTI-CMV-GFP-TREX1	Mohr et al., 2021	Addgene #164228
pTRIP-SFFV-EGFP-FLAG-cGAS E225A/D227A	Raab et al., 2016; Gentili et al., 2019	Addgene #127661
pTRIP-CMV-mCherry-FLAG-cGAS E225A/D227A	Gentili et al., 2019	Addgene #127657
pTRIP-SFFV-EGFP-53BP1	Lab of Dr. Nicolas Manel, Institut Curie, Paris	N/A
pLENTI-CMV-GFP-TREX1 deltaC (aa1-235)	Mohr et al., 2021	Addgene #164229
pLENTI-CMV-GFP-TREX1 deltaC-sec61TM	Lab of Dr. John Maciejowski, MSKCC, NY	N/A
pQCXIP-GFP-RPA70	Mohr et al., 2021	Addgene #164231
Software and algorithms		
GraphPad Prism version 5.02	GraphPad	https://www.graphpad.com/
Fiji ImageJ 1.52p	ImageJ	https://fiji.sc/
ImageJ macros	This paper	Mendeley Data https://doi.org/10.17632/hbhv5brnxj.1
Metamorph version 7.7.11.0	Molecular Devices, LLC	https://www.moleculardevices.com/

RESOURCE AVAILABILITY

Lead contact
Further information and requests for resources and reagents should be directed to and will be fulfilled by the lead contact, Matthieu Piel (matthieu.piel@curie.fr)

Materials availability

All newly generated materials associated with this study (stable cell lines and plasmids, design of microfabricated devices) will be provided upon request to the lead contact.

Data and code availability

All data reported in this paper will be shared by the lead contact upon request

All original code (ImageJ macros) has been deposited at Mendeley data and is publicly available as of the date of publication. DOIs are listed in the Key resources table.

Any additional information required to reanalyze the data reported in this manuscript is available from the lead contact upon request.

EXPERIMENTAL MODEL AND SUBJECT DETAILS

Mice

Animal care and use for this study were performed in accordance with the recommendations of the European Community (2010/63/ UE) for the care and use of laboratory animals. All animal experimental procedures were approved by ethics committee of Institut Curie CEEA-IC #118 (Authorization APAFiS #24649-2020031220398710-v1 given by National Authority) in compliance with international guidelines. As research was limited to the mammary gland, all transplanted animals were female mice.

Intraductal transplantation method

Eight to ten week-old virgin female CB17/Icr-Prkdc^{scid}/IcrIcoCrl mice (Charles River Laboratories) were anesthetized by inhalation with isoflurane and intraductally injected into the 3rd and the 4th pair of glands with 2 μL PBS containing 50,000 MCF10DCIS.com cells as previously described (Behbod et al., 2009; Lodillinsky et al., 2016). Five to eight weeks after injection with no additional manipulation, mice were sacrificed and the engrafted mammary glands were harvested and processed for whole-mount and histological and IHC staining on tissue sections.

Human tissues

Human breast cancer tissue samples were collected according to the Helsinki Declaration and the study was approved by the University of Palermo Ethical Review Board (approval number 09/2018). The cases were classified according to the World Health Organization classification criteria of the tumors of the breast. All the tissue samples were from 7 adult female patients with breast ductal adenocarcinoma with an age range between 40 and 88 years old (histotypes *in situ* ductal adenocarcinoma, invasive ductal adenocarcinoma or both).

Human Cell lines

Cell lines are described in the Key resources table. MCF10DCIS.com and MDA-MB-231 cell lines were kindly provided by the lab of Dr. Philippe Chavrier (Institut Curie, Paris, France). MCF10DCIS.com cells were cultured in Advanced DMEM- F12 (GIBCO) medium supplemented with 2 mM glutamine, 5% horse serum and 1% penicillin and streptomycin (GIBCO #15140-122). MDA-MB-231 was maintained in L-15 culture medium (Sigma-Aldrich, St Louis, MO, USA) with 2mM glutamine (GIBCO, Cergy Pontoise, France) and 15% fetal bovine serum (GIBCO). MCF10A cells were cultured in DMEM-F12 (GIBCO) supplemented with EGF (20ng/ml) (Peprotech #AF-100-15), hydrocortisone (0.5μg/ml) (SIGMA #H0888), cholera toxin (100ng/ml) (SIGMA #C8052), Insulin (10μg/ml) (SIGMA #I9278), 5% horse serum and 1% penicillin and streptomycin. RPE1 cells were grown in DMEM-F12 Glutamax medium (GIBCO), supplemented with 10% FBS and 1% penicillin and streptomycin (GIBCO). All cells were maintained at 37°C in 5% CO$_2$, with the exception of MDA-MB-231 cells, which were maintained at 37°C in 1% CO$_2$.

METHOD DETAILS

Constructs

The following constructs were kindly provided by the laboratory of Dr. Nicolas Manel (Institut Curie, Paris, France): pTRIP-CMV-mCherry-TREX1 WT and D18N were cloned from pEGFP-C1-TREX1 (Addgene #27219). pTRIP-SFFV-EGFP-FLAG-cGAS E225A/D227A and pTRIP-CMV-mCherry-FLAG-cGAS E225A/D227A are described elsewhere (Gentili et al., 2019; Raab et al., 2016). pTRIP-SFFV-EGFP-53BP1 (amino acids 1224-1716 for isoform 1) was obtained by cloning from pTRIP-CMV-mCherry-53BP1 (Gentili et al., 2019). The following constructs were provided byb the laboratory of Dr. John Maciejowski (MSKCC, New York, USA): pLENTI-CMV-GFP-TREX1 deltaC (aa1-235), pLENTI-CMV-GFP-TREX1 deltaC-sec61TM and pQCXIP-GFP-RPA70 (Mohr et al., 2021).

Lentiviral particles production in 293FT cells and Lentivector transductions

Lentiviral particles were produced as previously described from 293FT cells (Lahaye et al., 2013). Lentiviral viral particles and viral-like particles were produced by transfecting 1 μg of psPAX2 and 0.4 μg of pCMV-VSV-G together with 1.6 μg of a lentiviral vector plasmid

per well of a 6-well plate. For cell transduction, 0.5x10^6 cells were plated in a 6 well plate in 1ml and infected with 2ml of fresh lenti-vector in the presence of 8 μg/ml of Protamine.

Quantitative RT-PCR analysis

Total RNA was extracted using the RNeasy Mini kit (QIAGEN) and quantified by NanoDrop to assess both concentration and quality of the samples. Reverse transcription was performed using the SuperScript VILO cDNA Synthesis kit from Invitrogen. Gene expression was analyzed by using the TaqMan Gene expression Assay (Applied Biosystems). 0.1 ng of cDNA was amplified, in triplicate, in a reaction volume of 25 μl with 10 pmol of each gene-specific primer and the SYBR Green PCR MasterMix (Applied Biosystems). Real-time PCR was performed on the 14 ABI/Prism 7700 Sequence Detector System (PerkinElmer/Applied Biosystems) using a pre-PCR step of 10 min at 95 °C, followed by 40 cycles of 15 s at 95 °C and 60 s at 60 °C. Specificity of the amplified products was confirmed by melting curve analysis (Dissociation Curve TM; Perkin Elmer/Applied Biosystems) and by 6% PAGE. Preparations with RNA template without reverse transcription were used as negative controls. Samples were amplified with primers for each target gene and GAPDH as a housekeeping gene. The cycle threshold C_t values were normalized to the GAPDH curve. PCR experiments were performed in triplicate and standard deviations calculated and displayed as error bars.

cGAMP extraction with methanol/water

Cells were seeded and treated the day after with HT-DNA (1μg/ml) for 7h. 1.5x10^6 cells were recovered and washed with PBS. Cell pellets were resuspended in 80% methanol and frozen at −80°C. To perform cGAMP extraction, pellets were frozen/thawed five times in liquid nitrogen (with vortexing steps between each cycle). Then the samples were centrifuged at 16000 g for 20 min at 4°C. Supernatants were recovered and dried in a speed vaccum drying in Savant DNA Speed Vac DNA 110 for 3 h at 65°C. Pellets were resuspended in 150μl of DNase/RNase sterile water. cGAMP concentration was obtained with the 2′3′-cGAMP ELISA Kit (Cayman Chemical) according the manufacturer instruction. cGAMP quantities were normalized to the number of cells extracted.

Generation of TREX1 CRISPR clones

The guideRNA (gRNA) targeting TREX1 was kindly provided by the lab of Titia De Lange (Rockefeller University, New York, USA): gTREX1, 5′-GAGCCCCCCCACCTCTC-(PAM)-3′. gRNA plasmid was co-transfected into target cells with an hCas9 expression plasmid (Addgene) by nucleofection (Lonza apparatus). 1x10^6 cells were mixed with electroporation buffer (freshly mixed 125 mM Na2HPO4, 12.5 mM KCl, 55 mM MgCl2 pH 7.75), 2 μg Cas9 plasmid, and 2 μg gRNA plasmid, transferred to an electroporation cuvette (BTX), and electroporated with program U-017 for RPE-1 cells or program D-023 for MCF10DCIS.com cells. Cells were then allowed to recover for 48 h before single cell FACs sorting into single wells of a 96 wells plate for single clone amplification and selection. Successful CRISPR/Cas9 editing was confirmed by both western blotting of the amplified cell colonies and analysis of indel size (using the ICE analysis toolbox (https://www.synthego.com/products/bioinformatics/crispr-analysis).

Duct-on-a-chip assay

Unlabeled type I collagen at 2.4 mg/ml (BD Biosciences, Cat. # 354236) was injected in the "collagen chamber" of the microfabri-cated duct-on-a-chip and incubated for 1h at 37°C. In the meantime cells were ressuspended in matrigel (SIGMA #E1270) at a concentration of 0.7x10^6 cells/μl and then 3 μl were injected in the "cells chamber." Images were acquired at the desired time points after injection to assess cell invasion into the "collagen chamber."

Human primary tumor samples

Sections 2.5/3 micron-thick were cut from paraffin blocks, dried, de-waxed and rehydrated. The antigen unmasking technique was performed using Target Retrieval Solutions pH6 at 98°C for 30 min. After neutralization of the endogenous peroxidase with 3% H$_2$O$_2$ and Fc blocking by a specific protein block, double-marker immunohistochemistry was carried out by incubation for 90 min at RT with the primary antibodies RAB5A (Abcam, 1:100, pH6) and γH2AX (Abcam, 1:1000, pH6). Staining was revealed using Novolink Polymer Detection Systems (Novocastra) and SuperSensitive Link-Label IHC Detection System Alkaline Phosphatase (Biogenex). DAB (3,3′- diaminobenzidine) and Vulcan Fast Red were used as substrate chromogens. The slides were counterstained with Harris hema-toxylin (Novocastra). All the sections were analyzed under a Zeiss AXIO Scope.A1 microscope (Zeiss, Germany) and microphotographs were collected using a Zeiss Axiocam 503 Color digital camera using the Zen2 imaging software.

Immunohistochemistry and spectral multiplex (processed using Bond RX automated-Leica)

Antibody reference: cGAS (D1D3G) Rabbit mAb #15102; Cell Signaling, Dilution: 1/50. Antigen retrieval: BOND Epitope Retrieval Solution 2 (Leica, AR9961; pH9) for 20 min; protein blocking: 5 min (protein block serum-free Dako #X0909); incubation: 1h at room temperature

For DAB staining, once immunostaining finished, slides were counterstained with hematoxylin before mounting with glycergel me-dium (Dako). Images were acquired using Digital Pathology slide scanner (Nanozoomer 2.5, Hamamatsu). For multiplex IF, immuno-staining was processed with Opal 7-Color IHC Kits (Akoya 23 Biosciences, NEL821001KT). HRP labeled Rabbit Polymer and TSA

opal fluorophores were incubated for 10 min each. Subsequently, slides were submitted to DAPI staining for 10 min, washed and coverslipped with Prolong Diamond Antifade Mountant (ThermoFisher) before image acquisition.

Histological and immunofluorescence analysis of mouse tissue sections

Whole-mount carmine and hematoxylin and eosin staining were performed as described (Teulière et al., 2005). To retrieve antigens on paraffin-embedded tissue samples, sections were incubated for 20 min in 10mM sodium citrate buffer, pH 6.0 at 90°C. After 1h incubation in 5% fetal calf serum, sections were incubated overnight with diluted primary antibodies, washed and further incubated for 2h at room temperature with appropriate secondary antibodies.

Indirect immunofluorescence microscopy

Samples were fixed with 4% paraformaldehyde, permeabilized with 0.1% Triton X-100 for 5 min and then incubated for 1h at room temperature with primary antibodies. Following three washes with PBS, samples were incubated with the appropriate secondary antibodies for 1h at room temperature. Samples were again washed three times with PBS and mounted with Fluoromount G (Molecular probes).

3D type I collagen degradation assay

For collagen degradation assessment followed by immunofluorescence analysis, glass bottom dishes (MatTek Corporation) were layered with 15 μL of a solution of 5 mg/ml unlabeled type I collagen (IBIDI Cat. # 50201) mixed with 1/20-40 volume of Alexa Fluor 647-labeled collagen. Polymerization was induced at 37°C for 3 min and complete medium was added. Cells were seeded onto the polymerized collagen layer and incubated for 1h at 37°C. The medium was then gently removed and two drops of a mix of Alexa Fluor 647-labeled type I collagen (10% final) and unlabeled type I collagen at 2.4 mg/ml (BD Biosciences, Cat. # 354236) were added on top of the cells (top layer). After polymerization at 37°C for 1.5h, 1 mL of medium was added to the MatTek dishes.

Transfection procedure and siRNA oligonucleotides

For RNA interference experiments, cells were transfected with siRNA oligonucleotides (Dharmacon) using Lipofectamine® RNAi-MAX reagent (Invitrogen) (RPE1 cells), or with Lullaby (OZ Biosciences, France) (MCF10A cells, MCF10DCIS.com cells and MDA-MB-231 cells) according to manufacturer's protocol. The following SMARTpool siRNAs were used: human TREX1 (Dharmacon, cat. # L-013239-02-0005), human MB21D1 (cGAS) (Dharmacon, cat. # L-015607-02-0005) and validated non-targeting siRNAs (Dharmacon, cat. # D-001810-10-20). Cells were analyzed 72 h post-transfection using standard western blot or immunofluorescence analysis protocols.

Drug treatments

The following pharmacological inhibitors and chemical compounds were used: Etoposide (DNA damaging agent, topoisomerase-II inhibitor; Cell Signaling, #2200), Doxorubicin (DNA damaging agent, topoisomerase-II inhibitor; Cell Signaling, #5927), GM6001 (pan-inhibitor of matrix metalloproteinases; Millipore, # CC1010), KU-55933 (ATM kinase inhibitor; Abcam, #120637).

Western blotting

Cells were collected and resuspended in Laemmeli buffer. Proteins were separated using sodium dodecyl sulfate polyacrylamide gel electrophoresis (SDS–PAGE, 4%–20%) and transferred onto nitrocellulose or PVDF membranes. Membranes were blocked with 5% BSA in Tris-buffered saline containing 0.05% Tween (TBS-Tween) for 1 h at room temperature, after which primary antibodies were added in TBS-Tween 5% BSA and incubated over night at 4°C. The membranes were subsequently washed in TBS-Tween after which secondary horseradish peroxidase conjugated antibodies (Jackson ImmunoResearch) were added in 5% BSA in TBS-Tween and incubated for 1 h at room temperature. After extensive washing in TBS-Tween ECL signal was recorded on a ChemiDoc Touch Biorad Imager.

Microfabrication-based confinement

Confinement using the "6 well confiner"

To obtain large quantities of confined cells for cell population or biochemical studies, cell confinement was performed using a version of the cell confiner adapted to multi-well plates (Liu et al., 2015). To make the polydimethylsiloxane (PDMS, RTV615, GE) microspacers (micropillars) at the desired height, 12 mm glass coverslips were plasma treated and then placed on top of a PDMS mixture (10/1 w/w PDMS A / crosslinker B) on the wafer molds (containing holes/micropillars, fabricated following standard photolithography procedures). The height of the micropillars determines the height for spatial confinement of cells between the coverslip and the substrate. The surface of the confining side was always treated with non-adhesive pLL-PEG (SuSoS, PLL(20)-g[3.5]-PEG(2)). After baking at 95°C for 15 min, coverslips with PDMS pillars were carefully removed from the wafers under isopropanol. They were then cleaned with isopropanol, well-dried, treated with plasma for 1 min, and treated with 0.5 mg/mL pLL-PEG in 10 mM pH 7.4 HEPES buffer for 1h at room temperature. Coverslips with PDMS pillars were rinsed and incubated in medium for at least 2 hours before confining the cells. The modified cover-lid of a multi-well plate was used to apply confining slides to cells. In this case, large PDMS pillars were stuck on the cover-lid of the multi-well plate to hold the confining slides containing a layer of

microfabricated micropillars. These large PDMS pillars push the confining slides from the top of the plastic 6 well cover-lid to confine the cells in 6 well glass/plastic bottom plates. The process of fabrication of these large pillars attached to the 6 well plate lid is as follows: the large PDMS pillars were fabricated by pouring a PDMS mixture (A:B = 35:1) into a custom-made metallic mold, removing bubbles under vacuum, then baking overnight at 80°C, and getting the pillars out of the mold with the help of small amount of isopropanol.

Live-cell imaging

Time-lapse recordings were acquired with 20x (NA 0.75) or 40x (NA 0.85) dry objectives using either an Eclipse Ti inverted microscope (Nikon) equipped with a Coolsnap HQ2 camera (Photometrics) or with an spinning-disc confocal microscope with a Yokogawa CSU-X1 spinning-disc head on a DMI-8 Leica inverted microscope equipped with a Hamamatsu OrcaFlash 4.0 Camera, a Nano-ScanZ piezo focusing stage (Prior Scientific) and a motorized scanning stage (Marzhauser). Both microscopes were controlled by MetaMorph software (Molecular Devices). All microscopes were equipped with an on-stage incubation chamber which maintained the temperature at 37°C and CO_2 concentration at 5% at all times. Image analysis was performed using ImageJ/Fiji software (NIH, https://rsb.info.nih.gov/ij/index.html) or MetaMorph software (Universal Imaging).

Measurements of γH2AX intensity relative to tumor edge in mice xenografts

For semi-automated analysis of nuclear γH2AX intensity in tissues as a function of distance from tumor edge, a macro was written and run on Fiji software. First, individual nuclear regions were obtained after thresholding using the DAPI channel. Subsequently, the tumor edge was manually defined on the image using the myoepithelial layer as the reference. Next, a map of the distance to the tumor edge was obtained. Finally, γH2AX intensity and the distance to the edge was measured for each nuclei of the tumor xenograft. Cells with strongly condensed chromatin (as assessed by DAPI staining) were excluded from the analysis as they could be either mitotic or apoptotic cells. Due to intensity variation between experiments, γH2AX intensities were normalized using Z scores. For each image, the distribution of the intensities of nuclei inside the tumor (> 30μm from the myoepithelial layer) and at the tumor edge (< 30μm from the myoepithelial layer) were fit using a Gaussian function to obtain an average nuclear intensity and a standard deviation. Thus, individual nuclei intensities were normalized as: Z score = (Nuclear Intensity-Average Nuclear Intensity)/Standard Deviation, to compare all experiments.
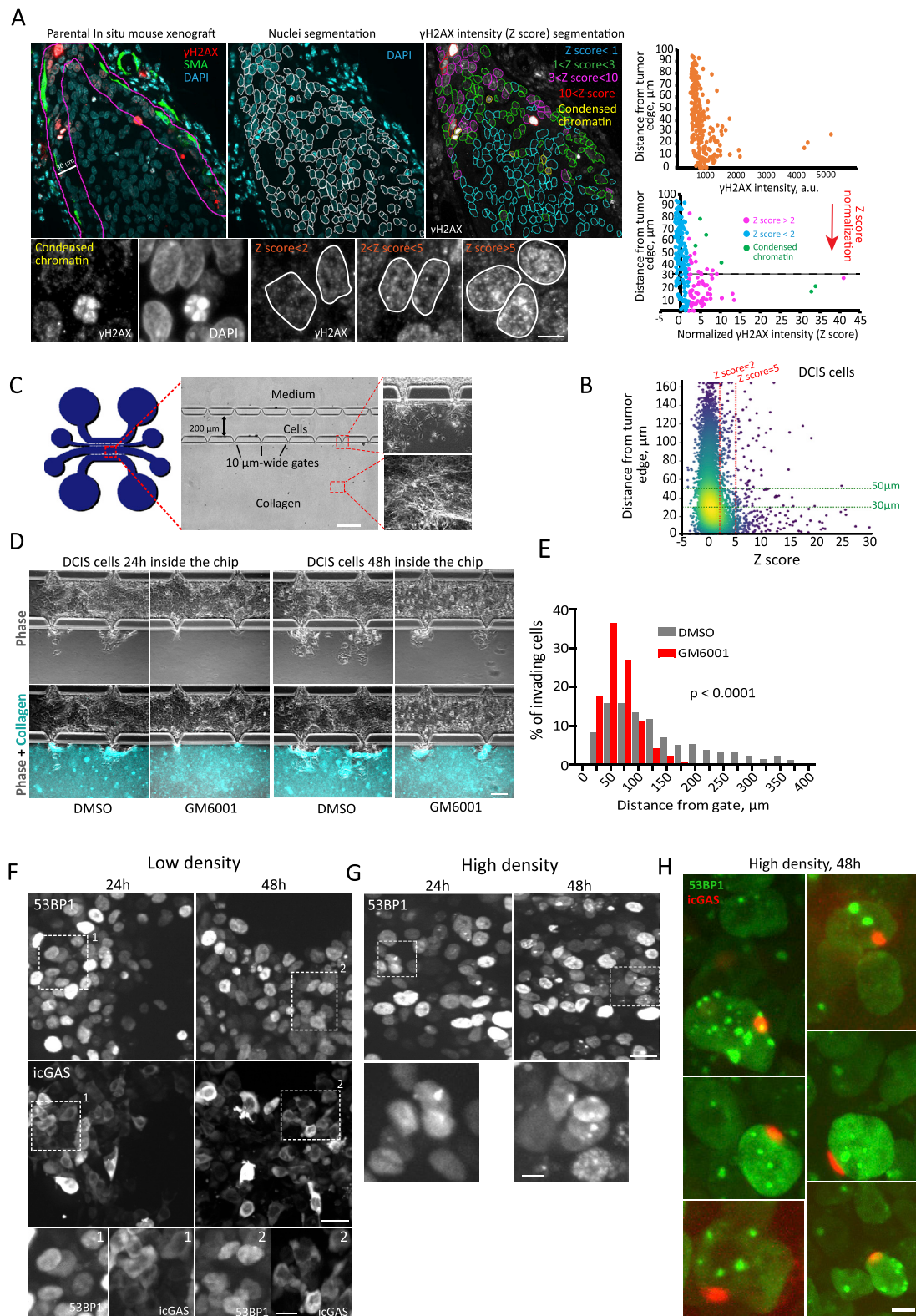
Electron microscopy

Sample preparation, ultrathin cryo-sectioning and immunolabelling were performed as previously described (Slot and Geuze, 2007). Briefly, RPE1 TREX1 KO + TREX1-mCherry were confined at 2 μm for 30 min. Next, the confinement lid was removed (in order to have enough number of cells for sample preparation, a total of twelve 6well plates were confined, cells were harvested and pooled together). Cells were harvested and processed for fixation for 2h with 2% formaldehyde + 0.125% Glutaraldehyde in 0.1 M phosphate buffer pH 7.4. The fixative was the replaced by PFA 1% in 0.1 M phosphate buffer and sample was stored at 4°C in a sealed tube. For the preparation of the blocks cells were rinsed with PBS, the blocks were embedded in 12% gelatin, cryoprotected with 2.3 M sucrose, and frozen in liquid nitrogen. Ultrathin cryo-sections were cut on a Leica ultracut UC7 cryomicrotome and picked up in a freshly prepared 1:1 mixture of 2.3 M sucrose and 1.8% methylcellulose, thawed and collected on formvar-coated grids. After washing with PBS containing 0.02 M glycine, sections were incubated with primary antibody (anti-mCherry; GeneTex #GTX 128508 used at 1:250 dilution and anti-PDI; EnzoLife Sciences ADI-SPA-891) and protein A-gold conjugates (PAG) (Utrecht University, the Netherlands). Sections were examined using a Tecnai Spirit electron microscope (FEI Company) equipped with a digital camera Quemesa (SIS). Quantitative Immuno EM analysis was used as described by Mayhew (2011). *Approach 1: Testing for shifts in compartment labeling in different groups of cells.* This approach is used to test whether the distribution of gold particles across compartments alters between not confined and 2 μm confined cells. The observed numerical frequency distributions of raw gold counts in different groups of cells are compared directly by contingency table analysis. For a particular compartment in a given cell, the number of expected gold particles is calculated by multiplying the corresponding column sum by the corresponding row sum and then dividing by the grand row sum (see Table S1). *Approach 2: Relative labeling index analysis, testing for differences in specific-labeling enrichment of TREX1-mCherry gold particles between cellular compartments.* Labeling density values relate numbers of gold particles to the sizes of compartments. For the relative labeling index analysis, a total of four compartments, including "nucleus," "peripheral ER," "inner nuclear membrane" and "outer nuclear membrane" were selected to analyze the intracellular distribution of TREX1-gold particles. The expected distribution was obtained by superimposing to pictures an array of points that was generated digitally, and points (P) were counted in the selected compartments. Pictures were taken randomly with the only criterion of a well-preserved morphology. Gold particles on all sampled fields were counted and named as observed gold particles (Ngo). For each compartment, Ngo was compared with the expected numbers of gold particles (Nge, derived from the observed frequencies of points P). Labeling density (LD) is calculated as the number of gold particles per test point ($LD = Ngo/P$). For each compartment, relative labeling index $RLI = LD$ compartment/LD cell. $RLI = 1$ indicates random labeling while $RLI > 1$ indicates when compartments are preferentially labeled. By means of a two-sample Chi-square ($\chi 2$) analysis with two columns (Ngo) and (Nge) and c compartments (arranged in rows), two distributions were compared, the total and partial $\chi 2$ values were calculated, and whether to accept or reject the null hypothesis was decided (of no difference between distributions) for $c-1$ degrees of freedom. For any given compartment, the partial $\chi 2$ is calcu-

lated as $(Ngo-Nge)^2/Nge$. If the observed and expected distributions are different, examining the partial $\chi2$ values will identify those compartments that are mainly responsible for that difference. A convenient arbitrary cut-off is a partial $\chi2$ value accounting for 10% or more of total (Mayhew, 2011).

QUANTIFICATION AND STATISTICAL ANALYSIS

Statistical analyses for all experiments were performed in Prism (GraphPad) v5.02. Statistical data are presented as median or mean $\pm$ SEM, SD or 10-90 percentiles. Sample size (n), statistical tests used and p values are specified in the figure legends. Samples in most cases were defined as the number of cells counted/examined within multiple different fields of view on the same dish/slide, and thus represent data from a single sample within a single experiment that are representative of at least three additional independently conducted experiments.

Supplemental figures

A — Parental In situ mouse xenograft / Nuclei segmentation / γH2AX intensity (Z score) segmentation

B — DCIS cells

C — Medium / Cells / 10 µm-wide gates / Collagen

D — DCIS cells 24h inside the chip / DCIS cells 48h inside the chip

E

F — Low density

G — High density

H — High density, 48h

Figure S1. The "duct-on-chip" device: reconstitution of the mammary duct using microfabrication, related to Figure 1

(A) Schematic showing the nuclei segmentation and Z score transformation for the normalization of γH2AX intensities as a function of the distance from the tumor xenograft edge (defined by the myoepithelial layer). Note that the great majority of nuclei with Z score > 2 are detected within the first 30 μm from the tumor edge/myoepithelial layer. Cells with strongly condensed chromatin (as assessed by DAPI staining) were excluded from the analysis as they could be either mitotic or apoptotic cells. Zoom bars, 5 μm. (B) Density scatterplot of Z scores (γH2AX intensities) of DCIS parental tumors. Data represent a total of 23 images analyzed from 3 independent experiments (mice injections). (C) Diagram illustrating the duct-on-chip device. A mixture of cells and matrigel is injected in the "cell chamber" and type I collagen is injected in the collagen chamber. Subsequently, culture medium is injected in the "medium chamber." Note that cells invade toward the collagen chamber through 10 μm wide gates that recapitulate the breaches in the myoepithelial layer during *in vivo* cell invasion. Bar, 80 μm. (D) DCIS cells were injected in the duct-on-chip in the presence of DMSO (vehicle) or MMP pan inhibitor (GM6001, 40 μM). Cell invasion was measured as distance from the gates. (E) Frequency distribution of invading cells as a function of the distance invaded from the gate. Data represent 3 independent experiments where cells invading from 10 random gates (at 20x magnification) were analyzed per condition per experiment. Bar, 60 μm. (F-H) Duct-on-chip assay. DCIS cells stably expressing 53BP1-mCherry and catalytically inactive cGAS-EGFP (icGAS) were injected in the chip device at low (F) and high (G, H) densities. Images were acquired at the indicated time points. (H) Nuclei displaying both NE rupture events (discrete cGAS accumulation at the nuclear border) and augmented 53BP1 foci are shown. Bars, 50 μm (F, G); 5 μm (H); zoom bars 20 μm (F), 10 μm (G). *P value* was calculated by Chi-square test in "E."
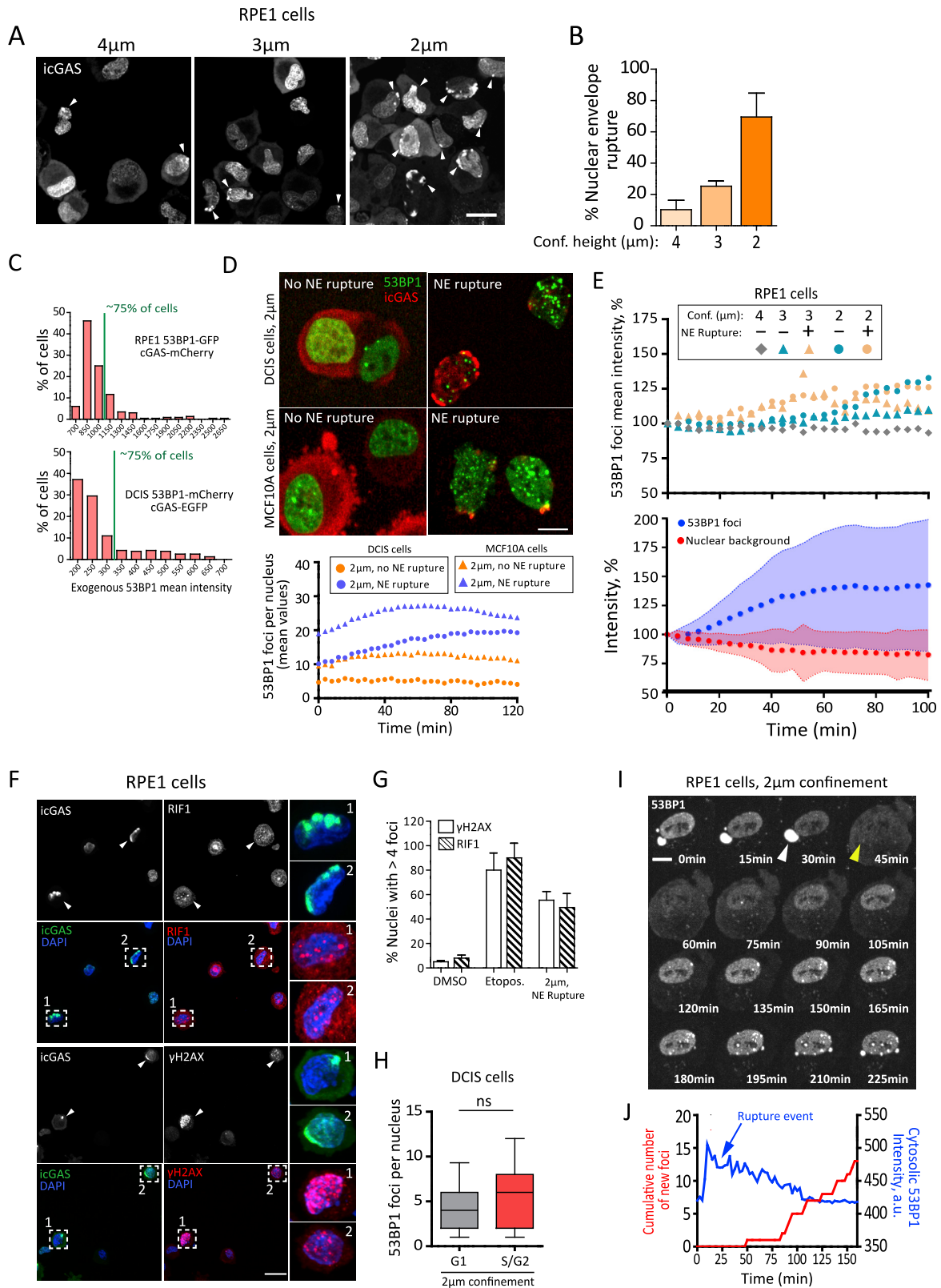
(legend on next page)

Figure S2. Characterization of nuclear envelope rupture under different confinement heights and of DNA damage following nuclear envelope rupture, related to Figure 2

(A) RPE1 cells stably expressing catalytically inactive cGAS-EGFP (icGAS) were confined at the indicated heights and images were acquired immediately after (and while cells were under confinement). Bar, 15 μm. (B) Quantification of NE rupture events as assessed by icGAS perinuclear localization. Data represent the mean $\pm$ SD of 3 independent experiments where 50 cells per experiment per height were analyzed. (C) Frequency distribution of 53BP1-EGFP (RPE1 cells, top) and 53BP1-mCherry (DCIS cells, bottom) mean intensities. (D) DCIS and MCF10A cells stably expressing 53BP1-mCherry and icGAS were confined at 2 μm. Top: examples of cells displaying or not NE rupture events (note perinuclear cGAS accumulation on cells displaying NE rupture). Bar, 10 μm. Bottom: quantification of DNA damage levels following 2 μm confinement as assessed by the number of 53BP1 foci in cells displaying or not NE rupture. Data represent the mean of 3 independent experiments (MCF10A cells) or 2 independent experiments (DCIS cells) where 20 cells per experiment per condition were analyzed. (E) Top: curves showing the 53BP1-EGFP mean intensity of RPE1 cells while under confinement at the indicated heights; data represent 4 independent experiments where 20 cells per experiment and per condition were analyzed. Bottom: curves showing the 53BP1-EGFP total intensity (blue) and the average nuclear background intensity (red) of RPE1 cells while under confined at 2μm. Data are pooled from 3 independent experiments where a total of 50 cells per condition were analyzed. Bars are SD. (F) RPE1 cells stably expressing icGAS were confined at 2 μm for 2 h; subsequently, the confinement lid was removed, cells were harvested, replated for 20 minutes and fixed for immunostaining with the DNA damage markers RIF1 and γH2AX (red) and DAPI (blue). Arrowheads point to cells with NE rupture, which are also positive for the DNA damage markers analyzed. Bar, 20 μm. (G) Quantification of DNA damage foci at the indicated conditions (DMSO, etoposide 25 μM and 2 μm confinement in cells displaying NE rupture). Images are representative of 2 independent experiments where 30 cells per experiment per condition were analyzed. Bars represent the mean $\pm$ SD. (H) DCIS cells stably expressing Geminin-mCherry and 53BP1-EGFP were confined at 2 μm and the number of 53BP1 foci was assessed; box and whisker plot shows the median value and 10-90 percentiles of 3 independent experiments where 20 cells per experiment per condition were analyzed. (I) RPE1 cells stably expressing 53BP1-EGFP were confined at 2 μm and imaged under spinning disc microscopy. White arrowhead points to a non-ruptured NE bleb while the yellow arrowhead points to a bleb bursting event that is followed by the appearance of DNA damage foci. Bar, 5 μm. (J) Graph showing the cumulative number of new 53BP1 foci (red curve) following a bleb bursting event (assessed by an increase in the cytosolic intensity of the probe 53BP1-EGFP, which leaks out of the nucleus upon NE rupture, blue curve). Blue arrow indicates the instant of NE rupture/bleb bursting. *P value* was calculated by unpaired Student's t test in "H"; ns = not significant.
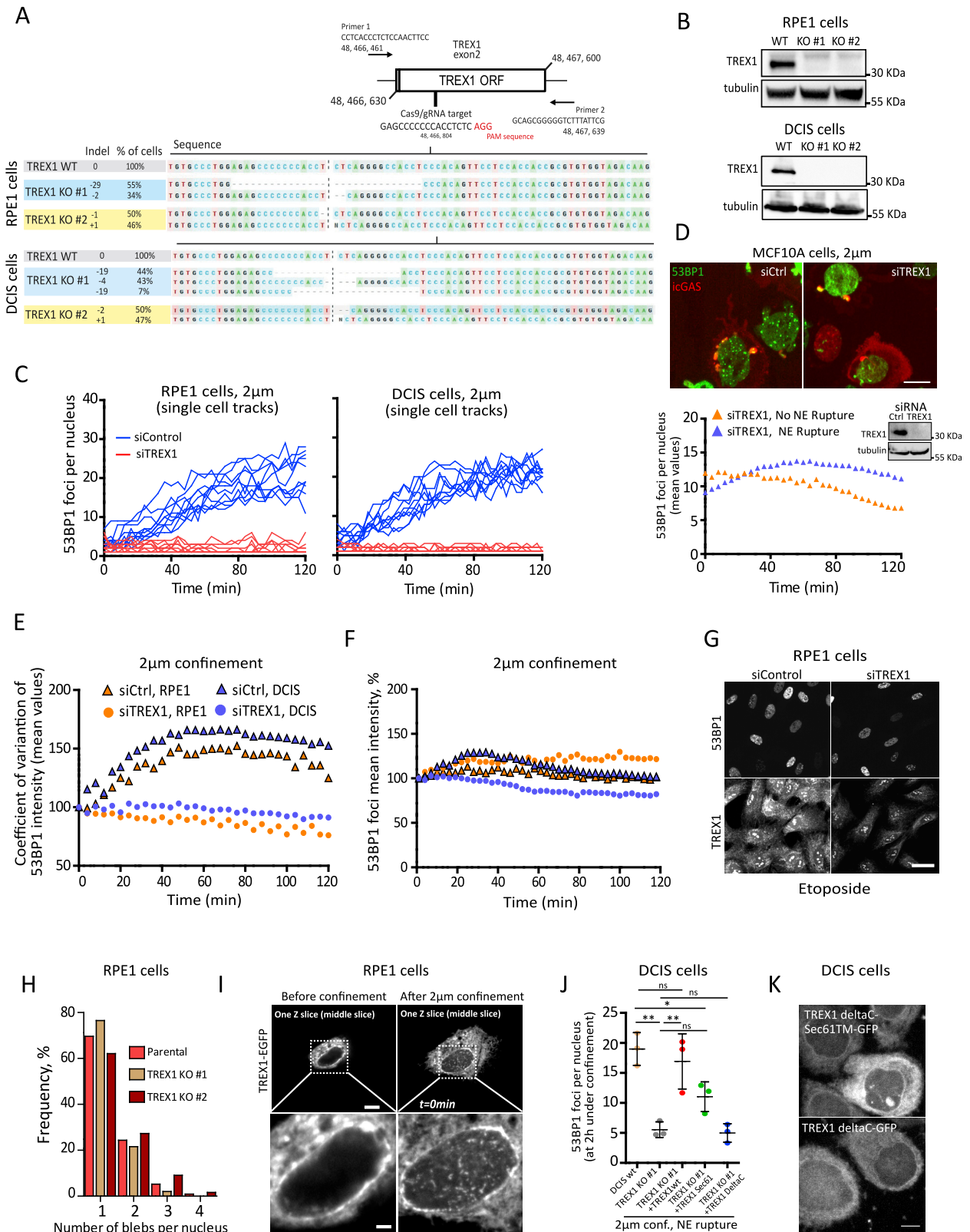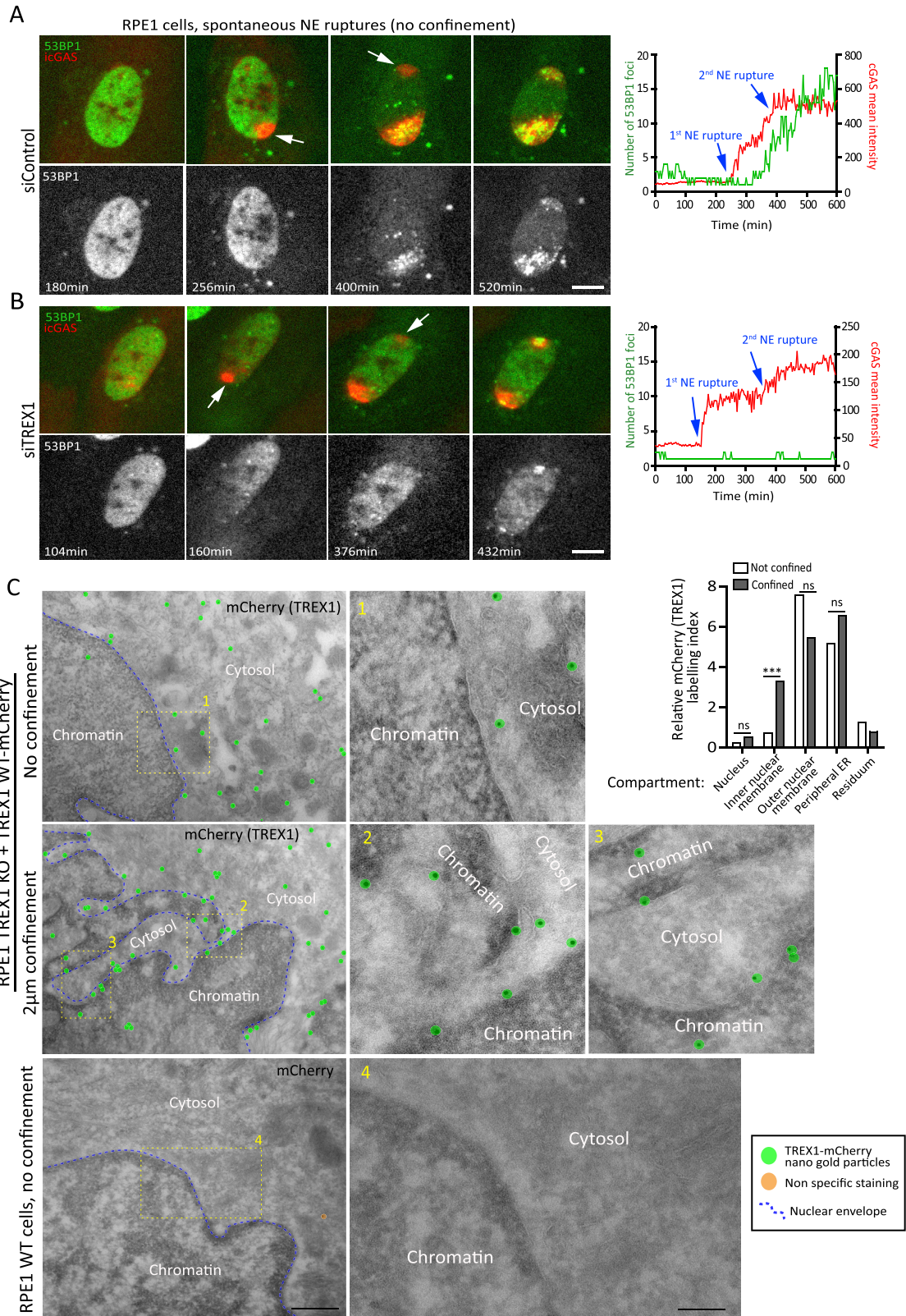
Figure S3. Characterization of DNA damage following nuclear envelope rupture in different cell lines and of TREX1 KO clones, related to Figure 3

(A) Diagrams illustrating the Cas9/gRNA targeting sequence in the *TREX1* gene and the primers used for the sequencing of the TREX1 KO clones generated by CRISPR technology for RPE1 and DCIS cells. (B) Western blot of DCIS/RPE1 TREX1 WT and DCIS/RPE1 TREX1 KO clones; tubulin is a loading control. (C) Single cell curves of 53BP1 foci number as a function of time in RPE1 cells (left) or DCIS cells (right) displaying NE rupture events while under 2 μm confinement. (D) Top: MCF10A cells stably expressing 53BP1-EGFP and catalytically inactive cGAS-mCherry (icGAS) were transiently depleted for TREX1 with siRNA and 48 h later cells were confined at 2 μm. Bottom: Quantification of DNA damage levels during 2 μm confinement as assessed by the number of 53BP1 foci in siTREX1 MCF10A cells displaying or not NE rupture. Western blot shows TREX1 depletion 48 h post-knockdown; tubulin is the loading control. Data represent the mean of 3 independent experiments where 20 cells per experiment per condition were analyzed. (E) Mean values of the ratio between 53BP1 foci SD mean intensity and 53BP1 foci mean intensity (coefficient of variation of 53BP1 foci intensity) of RPE1 and DCIS cells transiently depleted for TREX1 and confined at 2 μm. This is an alternative way of quantifying the increase in the number of 53BP1 foci in the nucleus, without counting the foci. This globally measures the coefficient of variation of the signal, which increases when the signal becomes less homogeneous. (F) Curves showing the 53BP1-EGFP mean intensity of RPE1 and DCIS cells transiently depleted for TREX1 and confined at 2 μm. (E, F) Graphs represent data pooled from 3 independent experiments for approximately 50 cells analyzed per condition. (G) RPE1 cells stably expressing 53BP1-EGFP were transiently depleted for TREX1 using siRNA and treated with etoposide (25 μM) for 2 h. Subsequently, cells were fixed and stained for endogenous TREX1. Bar, 25 μm. (H) Frequency distribution of the number of nuclear blebs in RPE1 TREX1 KO clones and in parental RPE1 cells. Data represent 3 independent experiments where 60 cells per experiment were analyzed. (I) RPE1 cells transiently transfected with TREX1-EGFP WT were confined at 2 μm using a pressure-controlled dynamic confiner. Images represent a single plane Z slice through the middle section of the nucleus. Bars, 5 μm and 1 μm (magnification). Images are representative of 2 independent experiments. (J) Quantification of DNA damage levels (number of 53BP1 foci) in parental DCIS cells and in DCIS TREX1 KO #1 cells stably expressing 53BP1-mCherry reconstituted with the indicated TREX1 constructs fused to GFP and confined at 2 μm. Quantification was performed in cells displaying NE rupture. Data represent the mean ± SD of 3 independent experiments where 25 cells per condition per experiment were analyzed. (K) Images showing the distribution of TREX1 deltaC-GFP and TREX1 deltaC-Sec61TM-GFP in DCIS TREX1 KO #1 cells confined at 2 μm (note the diffuse distribution of TREX1 deltaC-GFP). Bar, 5 μm.

A RPE1 cells, spontaneous NE ruptures (no confinement)

siControl
53BP1
icGAS
53BP1
180min 256min 400min 520min

2nd NE rupture
1st NE rupture

B
siTREX1
53BP1
icGAS
53BP1
104min 160min 376min 432min

1st NE rupture
2nd NE rupture

C
RPE1 TREX1 KO + TREX1 WT-mCherry
No confinement
mCherry (TREX1)
Cytosol
Chromatin

2μm confinement
mCherry (TREX1)
Cytosol
Chromatin

RPE1 WT cells, no confinement
mCherry
Cytosol
Chromatin

Not confined
Confined

Compartment: Nucleus, Inner nuclear membrane, Outer nuclear membrane, Peripheral ER, Residuum

TREX1-mCherry nano gold particles
Non specific staining
Nuclear envelope

(legend on next page)

Figure S4. Characterization of DNA damage following spontaneous nuclear envelope rupture and TREX1 localization by electron microscopy, related to Figure 3

(A, B) Left: RPE1 cells stably expressing 53BP1-EGFP and catalytically inactive cGAS-mCherry (icGAS) were transiently transfected with a non-coding siRNA (A) or with a siRNA targeting TREX1 (B), plated on glass bottom dishes and imaged for several hours. Arrows point to NE rupture events (note the accumulation of the icGAS signal at the rupture site). Right: curves showing the relationship between NE rupture and the appearance of 53BP1 foci (note that in TREX1-depleted cells 53BP1 foci number remains low following NE rupture events). Bars, 5 μm. (C) Immuno-gold electron microscopy images of non-confined (top panels) and confined (2 μm, middle panels) RPE1 TREX1 KO cells reconstituted with TREX1-mCherry. Bottom panels: non-confined RPE1 WT cells. Following confinement, cells were harvested and labeled with an antibody against mCherry to detect either transduced TREX1 (top and middle panels) or non-specific labeling (negative control, bottom panels). Graph shows the quantification of the relative labeling index (see methods for detailed explanation) of mCherry (TREX1) immune gold particles at the indicated cellular compartments. Bar, 0.5 μm; magnified regions bar, 0.1 μm. For the graph of panel "C," refer to methods and Table S2 for the complete set of numbers and statistics, *** does not stand for P value but significance according to the chi-square statistics. A total of 6 pictures from not confined (260 gold particles) and 9 pictures from 2 μm confined cells (303 gold particles) were used for quantification; ns = not significant. See also Table S2 and Video S4.

A RPE1 cells   MCF10A cells   DCIS cells

B RPE1 cells

C RPE1 cells, 2μm

D RPE1 cells
2μm confinement, 12h

E RPE1 cells

F MCF10A cells, 12h confinement
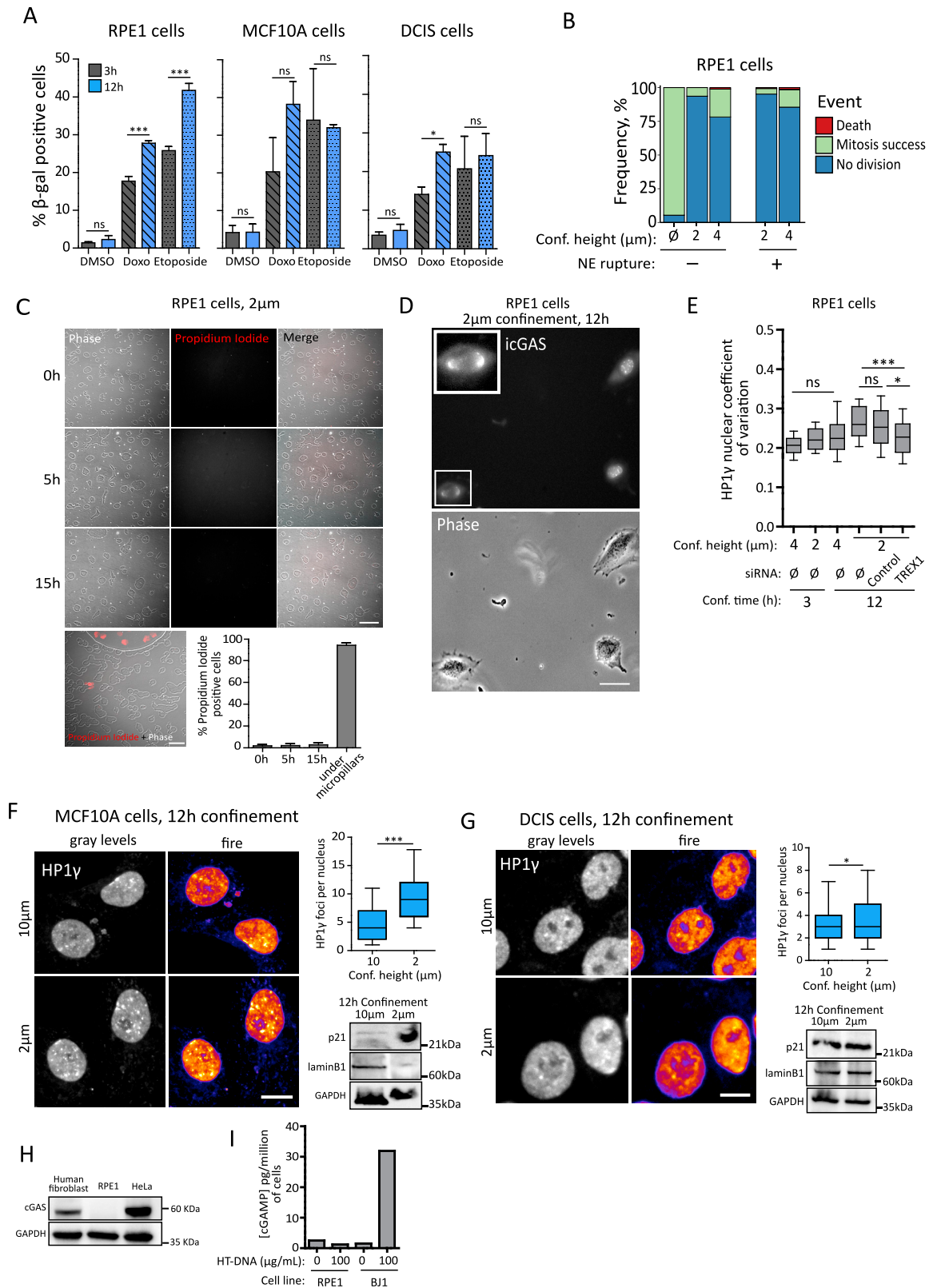
G DCIS cells, 12h confinement

H

I

Figure S5. Long-term, strong confinement causes cell senescence in non-transformed cells but not in cancer cells, related to Figure 4

(A) RPE1, MCF10A and DCIS cells were treated with doxorubicin (40 nM), etoposide (25 μM) or DMSO (vehicle) for the indicated lengths of time. Cells were then fixed and processed for β-gal staining. The percentage of β-gal-positive cells was plotted. Graph, data represent mean ± SD of 3 independent experiments where 200 cells were scored per condition per experiment. (B) Frequency distribution of the designated categories for cells under the indicated confinement heights. Data represent 3 independent experiments where 37 non-confined cells, 40 confined cells with non-ruptured nuclei and 60 confined cells with ruptured nuclei were scored per condition per experiment. (C) RPE1 cells were confined at 2 μm in the presence of Propidium Iodide and imaged overnight. Graph, data represent the mean ± SD of 3 independent experiments where 5 random fields (at 20x magnification) were scored per time point per experiment. Bar, 50μm. (D) Epi-fluorescence and phase images of RPE1 cells stably expressing catalytically inactive cGAS-EGFP (icGAS) harvested from 2 μm confinement and replated for cell cycle duration measurement over a 72 h period. Bar, 25 μm. Inset shows a cell with ruptured NE, as evidenced by icGAS perinuclear accumulation. (E) Graph: box and whisker plot showing the median value and 10-90 percentiles of the ratio between the SD of heterochromatin foci (HP1γ) intensity and HP1γ mean intensity (coefficient of variation). This is an alternative way of quantifying the increase in the number of HP1γ foci in the nucleus, without counting the foci. This globally measures the coefficient of variation of the signal, which increases when the signal becomes less homogeneous. Data represent 3 independent experiments where 70 cells were scored per condition per experiment. (F) MCF10A cells or (G) DCIS cells were confined for 12 h at 10 or 2 μm, harvested from confinement and replated for 72 h before fixation for immunostaining with HP1γ antibody or lysis for western blot analysis of lamin B1 and p21. GAPDH is the loading control. Western blot images are representative of 2 independent experiments. Graph, box and whisker plot showing the median value and 10-90 percentiles of the number of HP1γ foci per nucleus. Data represent 3 independent experiments where 100 cells per condition per experiment were analyzed. Bars, 10 μm. (H) Western blot analysis of whole cell extracts of human fibroblasts, RPE1 cells and HeLa cells. GAPDH is the loading control. (I) cGAMP measurements for the indicated cells lines. Bars represent 1 experiment that was performed in duplicate. *P value*s were calculated by One-way ANOVA with post hoc Tukey test (A and E) or unpaired Student's t test (F, G). ***p < 0.0001; *p < 0.05; ns = not significant.
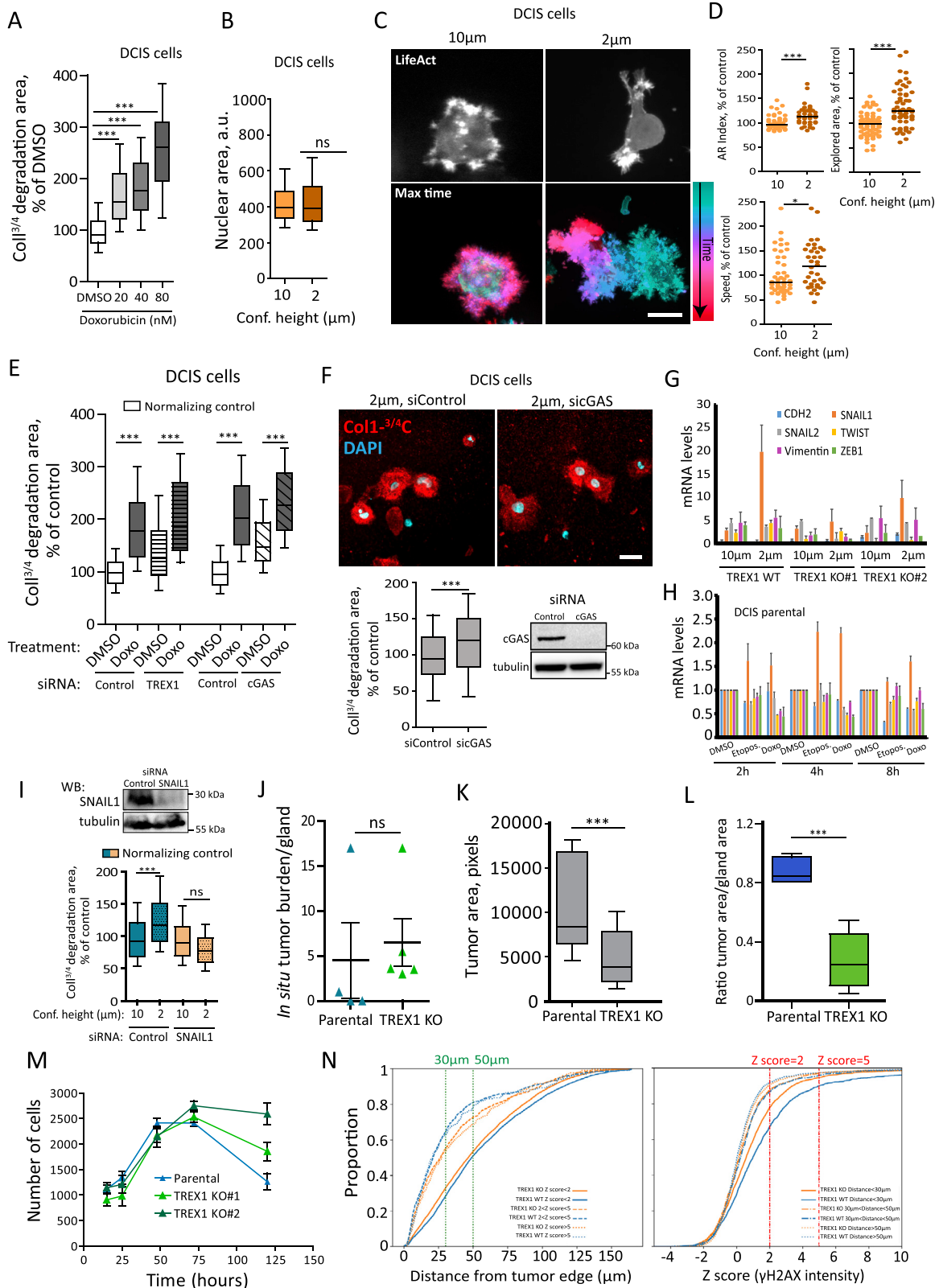
Figure S6. Pharmacologically induced DNA damage promotes collagen degradation independently of both TREX1 and cGAS and strong confinement induces cell polarization and collagen degradation in a cGAS-independent fashion. TREX1 KO clones display normal prolif-eration both *in vitro* and *in vivo*, related to Figures 5 and 6

(A) DCIS cells were treated for 12 h with the indicated concentrations of doxorubicin or DMSO (vehicle). Following the incubation period, cells were harvested and embedded in 3D type I collagen for 12 h to assess their collagen degradation activity by immunostaining with an antibody that specifically recognizes the collagenase-cleaved $^3/_4$ fragment of collagen I. Graph, box and whisker plot showing the median value and 10-90 percentiles of the collagen degradation area. Data was normalized by the mean of control (DMSO) samples. Data represent 3 independent experiments where 50 cells per condition per experiment were analyzed. (B) Quantification of nuclear area of DCIS cells embedded into 3D type I collagen following the indicated confinement heights. Graph, box and whisker plot showing the median value and 10-90 percentiles of nuclear projected area. Data represent 3 independent experiments where 70 cells per condition per experiment were analyzed. (C) DCIS cells stably expressing life Act-EGFP were confined for 2 h at the indicated heights. Following the confinement period, cells were harvested and embedded in 3D type I collagen and imaged for 15 h. Bar, 20 μm. (D) Scatter dot plots of different measured parameters while cells where embedded into 3D type I collagen (lines are median). Data represent 2 independent experiments where 25 cells per condition per experiment were analyzed. (E) DCIS cells were transiently depleted for TREX1 or cGAS using siRNA and 48 h later cells were pre-treated for 12 h with doxorubicin (Doxo, 80 nM) or DMSO (vehicle). Following the treatment period, cells were harvested and embedded in 3D type I collagen for 12 h to assess their collagen degradation activity by immunostaining with an antibody that specifically recognizes the collagenase-cleaved $^3/_4$ fragment of collagen I. Graph, box and whisker plot showing the median value and 10-90 percentiles of the collagen degradation area. Data was normalized by the mean of control samples. Data represents 3 independent experiments where 40 cells per condition per experiment were analyzed. (F) DCIS cells were transiently depleted for cGAS using siRNA and 48 h later cells were confined at 2 μm for 2 h. Following the confinement period, cells were harvested and embedded in 3D type I collagen for 12 h to assess their collagen degradation activity by immunostaining with an antibody that specifically recognizes the collagenase-cleaved $^3/_4$ fragment of collagen I (red); DAPI (cyan). Bar, 20 μm. Graph, box and whisker plot showing the median value and 10-90 percentiles of the collagen degradation area. Data was normalized by the mean of siControl sample. Data represent 3 independent experiments where 60 cells per condition per experiment were analyzed. Western blot shows cGAS depletion (48 h post-knockdown); tubulin is a loading control. (G) Quantitative Real Time-PCR analysis. DCIS wt or DCIS TREX1 KO clones were confined at the indicated heights for 2 h. Cells were harvested, lysed and processed for analysis of the expression of mRNAs of EMT markers. (H) DCIS wt cells were treated for the indicated lengths of time with DMSO (vehicle), Doxorubicin (80 nM) or Etoposide (100 μM). Cells were harvested, lysed and processed for analysis of the expression of mRNAs of EMT markers. Data represent the mean ± SD of 3 independent experiments with 3 replicates per experiment. (I) DCIS wt cells were transiently depleted for SNAIL1 and confined at the indicated heights for 2 h. Following the confinement period, cells were harvested and embedded in 3D type I collagen for 12 h to assess their collagen degradation activity by immunostaining with an antibody that specifically recognizes the collagenase-cleaved $^3/_4$ fragment of collagen I. Graph, box and whisker plot showing the median value and 10-90 percentiles of the collagen degradation area. Data was normalized by the mean of control samples. Data represent 3 independent experiments where 60 cells per condition per experiment were analyzed. Western blot shows SNAIL1 depletion 48 h post-knockdown; tubulin is the loading control. (J) Graph showing the rate of *in situ* tumor burden (period of 6-8 weeks post-intraductal injection). Data represent the mean ± SEM. A total of 4 parental and 11 TREX1 KO glands were analyzed. (K) Graph, box and whisker plot showing the median value and 10-90 percentiles of the tumor area generated by DCIS parental or TREX1 KO clones (6-8 weeks post-intraductal injection). (L) Graph: box and whisker plot showing the median value and 10-90 percentiles of the ratio between tumor area and gland area generated by DCIS parental or DCIS TREX1 KO clones (6-8 weeks post-intraductal injection). Data represent a total of 7 glands scored for DCIS parental tumors and 14 glands for TREX1 KO tumors. (M) Proliferation curve of DCIS parental and DCIS TREX1 KO #1 and TREX1 KO #2 clones. Graph, data represent the mean ± SEM of 25 random fields scored at 20x magnification. (N) Graphs showing the proportion of nuclei as a function of distance from the tumor edge (left) or Z score (γH2AX intensities) (right) for mice tumor xenografts generated by injection with either DCIS parental cells or DCIS TREX1 KO clones. Data represent a total of 23 images analyzed for DCIS parental tumors and 30 images for TREX1 KO tumors (TREX1 KO #1 +TREX1 KO #2 clones) from 3 independent mice injections. *P value*s were calculated by unpaired Student's t test (B, D, F, I, J-L), One-way ANOVA with post hoc Tukey test (A, E). ***p < 0.0001; *p < 0.05; ns = not significant. See also Video S5.

A DCIS cells

B Human invasive breast ductal carcinoma

C Hydroxyurea 2mM   3μm confinement

D DCIS cells

E DCIS cells

F TREX1 mRNA expression (RNAseq)

HR= 2.24 (1.6 - 3.13)
logrank P= 1.4e-06

G MDA-MB-231 cells, 2μm

H

I Human colorectal cancer

J Human colon rectal cancer, invasive margin
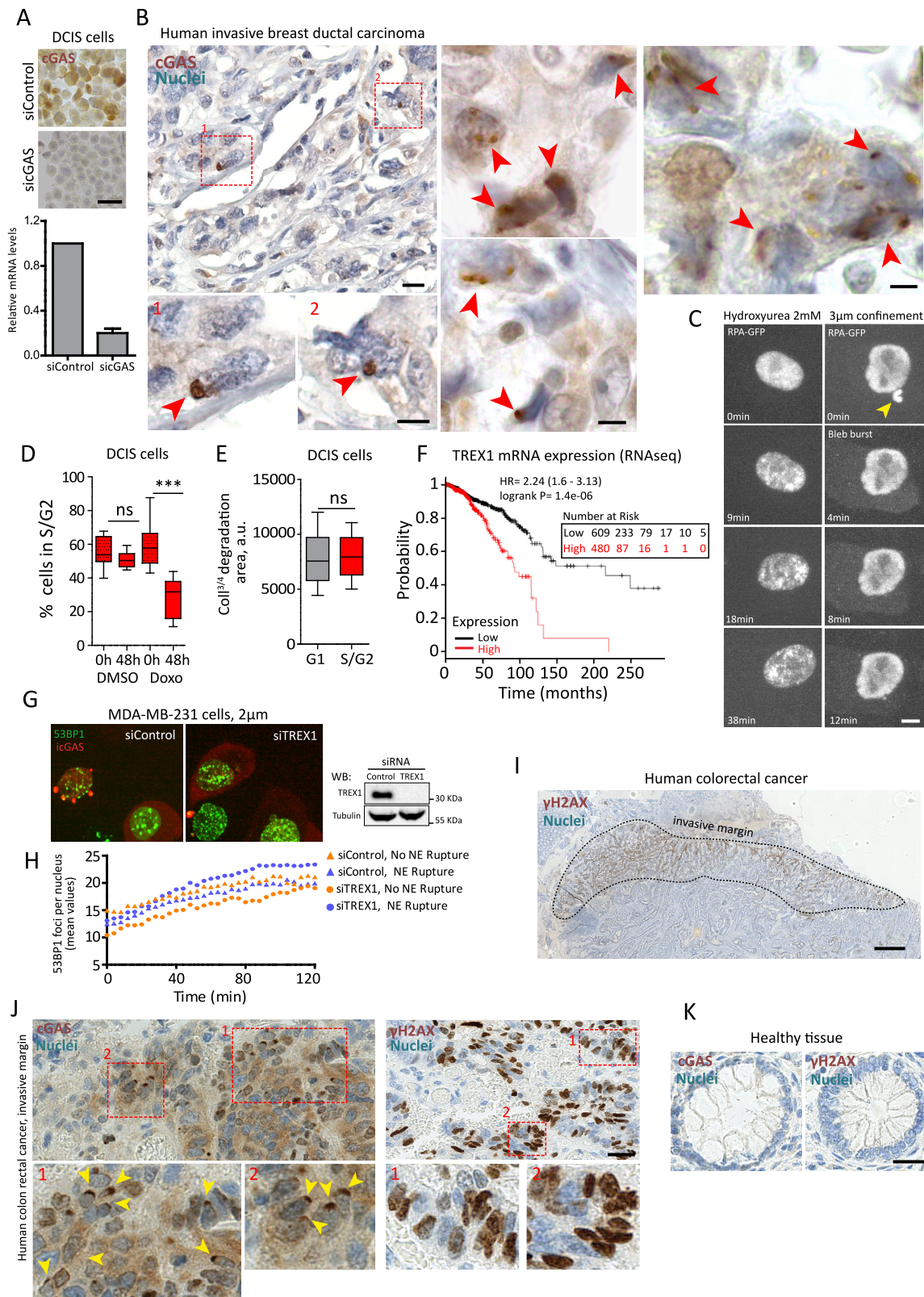
K Healthy tissue

Figure S7. Additional results commented in the discussion of the article, including analysis of TREX1 expression that reveals poor prognosis in breast cancer and cGAS staining in human tumor samples, related to Figure 7

(A) cGAS antibody validation by immunohistochemistry (IHC). (Top) DCIS were transiently transfected with siRNA control or siRNA cGAS and 72 hour later cells were paraffin embedded and formalyin fixed for IHC processing. Bar, 40 μm. (Bottom) Quantitative RT-PCR showing cGAS mRNA levels (relative to siControl-treated cells). (B) cGAS immunohistochemistry (brown) and nuclei (blue) in overtly invasive human breast ductal carcinoma. Insets 1 and 2: note cGAS accumulation at the tip of ruptured nuclei. Red arrowheads point to NE rupture events. Left panels: bar, 25 μm and inset, 3 μm; middle panels: bar, 8 μm; right panels: bar, 3 μm. (C) RPE1 cells were transiently transfected with RPA-GFP and either treated with hydroxyurea 2mM or confined at 3 μm and imaged for several minutes. Yellow arrowhead points to a nuclear bleb that eventually bursts. Bar, 10 μm. (D) DCIS cells stably expressing Geminin-mCherry were treated with DMSO (vehicle control) or doxorubicin (40 nM) and the percentage of cells in S/G2 was assessed at 0 h and 48 h of treatment; box and whisker plot shows the median value and 10-90 percentiles of 2 independent experiments where at least 400 cells per experiment per condition were analyzed. (E) DCIS cells stably expressing Geminin-mCherry were embedded in 3D type I collagen for 12 h to assess their collagen degradation activity by immunostaining with an antibody that specifically recognizes the collagenase-cleaved $^3/_4$ fragment of collagen I; box and whisker plot shows the median value and 10-90 percentiles of 2 independent experiments where at least 100 cells per experiment were analyzed. (F) Kaplan Meier survival plot for patients expressing low (black line) and high (red line) levels of TREX1 mRNA obtained by RNaseq. Data was obtained from The Cancer Genome Atlas (TCGA), https://kmplot.com. (G) MDA-MB-231 cells stably expressing 53BP1-EGFP and catalytically inactive cGAS-mCherry (icGAS) were transiently depleted for TREX1 and confined at 2 μm. Bar, 10 μm. (H) Quantification of DNA damage levels following 2 μm confinement as assessed by the number of 53BP1 foci in MDA-MB-231 cells displaying or not NE rupture (siControl and siTREX1). Data represent the mean of 2 independent experiments where 20 cells per experiment per condition were analyzed. Western blot shows TREX1 depletion 48 h post-knockdown; tubulin is the loading control. (I) Overview of immunohistochemistry analysis of moderately differentiated human colon rectal adenocarcinoma, infiltrating until muscle layer with perineural invasion (classification: pT2). γH2AX (brown) and nuclei (blue). Bar, 1mm. (J) Magnified regions of the invasive margin shown in "I." (Left) Immunohistochemistry of cGAS (brown) and nuclei (blue). Yellow arrowheads point to NE rupture events. (Right) Immunohistochemistry of γH2AX (brown) and nuclei (blue). Bar, 20 μm. (K) Magnified regions of the healthy tissue from the same patient. Bar, 20 μm. *P value*s were calculated by unpaired Student's t test, ***p < 0.0001; ns = not significant.